

Simulation of Passive Imaging of Underwater Objects

A. Kouzoubov

DSTO-TR-1240

20020129 142

Simulation of Passive Imaging of Underwater Objects

Alexei Kouzoubov

Maritime Operations Division
Aeronautical and Maritime Research Laboratory

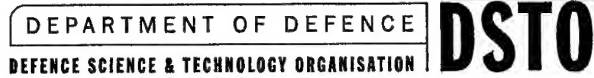
DSTO-TR-1240

ABSTRACT

A computer model simulating performance of passive optical sensors for imaging underwater objects from above-water platforms is described. The model is based on the models of sun and sky spectral radiance, wavy sea surface, light propagation in seawater and is able to render images of underwater objects as seen through the air-water interface.

RELEASE LIMITATION

Approved for Public Release.



AQ F02-04-0652

Published by

*DSTO Aeronautical and Maritime Research Laboratory
506 Lorimer St
Fishermans Bend, Victoria 3207 Australia*

*Telephone: (03) 9626 7000
Fax: (03) 9626 7999
© Commonwealth of Australia 2001
AR-012-070
November 2001*

APPROVED FOR PUBLIC RELEASE

Simulation of Passive Imaging of Underwater Objects

Executive Summary

A computer model has been developed to simulate the performance of passive optical imaging sensors, such as a human eye, a conventional digital camera or a hyperspectral sensor. The model is based on the ray tracing technique and it implements several basic models describing various elements of image formation. These models are an analytical model of sun and sky radiance, a model of wind driven waves on the sea surface based on the directional wave spectrum, a sun and sky reflection model by capillary waves on the sea surface, and a bio-optical model of seawater. Several empirical and semi-empirical relations are used for describing such elements as radiance and irradiance transfer through a wavy sea surface, image blur due to light scattering in ocean water etc. An analytical expression for radiance scattered into a ray path has been developed in the present work.

All these models are based on approximations of various degrees of accuracy. Some of them were verified in the present work against other models and ground truth measurements. The model produces realistic images of sea surface and underwater targets but further verification of the simulation model and its components is required and planned in the near future. The work will include comparison of simulations with hyperspectral data and ground truth measurements. Further improvements to the model elements will be made. It is planned to expand the model to incorporate simulation of the performance of active imaging systems such as Laser Range Gated (LRG) cameras and the Streak Tube Imaging Lidar (STIL). Also, atmospheric effects on light propagation near the sea surface will be included in the model.

The verified model may be used for estimating performance of optical sensors in various scenarios of underwater object detection. Output of the model may provide input for such areas of operations research as mine hunting and amphibious operations.

Authors

Alexei Kouzoubov
Maritime Operations Division

Alexei Kouzoubov is a Senior Research Scientist. He has a PhD in Computational Fluid Dynamics from the Institute for High Temperatures of Russian Academy of Sciences. He has previously worked at Universities of Adelaide, New South Wales, and South Australia before joining DSTO in 1998. His current interest is in ocean optical modelling with application to optical detection of underwater objects and simulation of performance of optical systems in maritime environment.

Contents

1. INTRODUCTION.....	1
2. SIMULATION SOFTWARE DESIGN.....	2
3. SUN AND SKY RADIANCE MODEL.....	5
4. SEA SURFACE MODEL.....	9
5. RADIANCE REFLECTED FROM SEA SURFACE.....	10
6. RADIANCE FROM BELOW SEA SURFACE.....	10
7. BIO-OPTICAL MODEL.....	18
8. TARGET RENDERING	25
9. SENSOR MODEL	27
10. SIMULATION EXAMPLES	28
11. CONCLUSION.....	32
12. ACKNOWLEDGMENTS	33
13. REFERENCES	33
APPENDIX A:ANALYTICAL MODEL OF SKY RADIANCE	37
APPENDIX B:WAVENUMBER SPECTRUM.....	43
APPENDIX C: BIO-OPTICAL MODEL.....	45

1. Introduction

Maritime Operations Division of DSTO is currently assessing various electro-optical techniques, both passive and active, for underwater object detection. Although the final word in such an assessment belongs to experiment the initial estimation of a system performance can be made via simulation based on a physically correct model of image transfer through water and the air-sea interface. Another advantage of such a model is that, once verified, it can be used for estimation of sensor performance under various operational conditions where real experiment may be expensive.

A model is currently being developed for simulating images of underwater objects as seen by various types of optical sensors, both passive and active. The simulation model is based on physically accurate models of sun and sky radiance, wind generated waves on the sea surface, and the optical properties of ocean water. The model can generate images of a three-dimensional object constructed from simple geometrical objects such as cylinders, spheres, cones etc. It can also take as input any digital image and simulate its degradation due to scattering in water and through the wavy sea surface. This report describes the model implementation for passive imaging sensors and presents the results of simulations.

The geometry and main features of the passive sensor model are shown in Figure 1. The simulation of an image is based on the ray tracing technique. Rays are traced from each pixel in the image plane and radiance towards the receiver is calculated in the ray path. The direction of rays in water is calculated from Snell's law applied to a wavy sea surface. Since the model simulates a passive sensor an accurate model of natural illumination plays an important role. The path radiance in an individual field of view is the sum of sun and sky radiance reflected from the sea surface, backscattered from water, reflected from the bottom, and reflected from a target if the ray crosses the target.

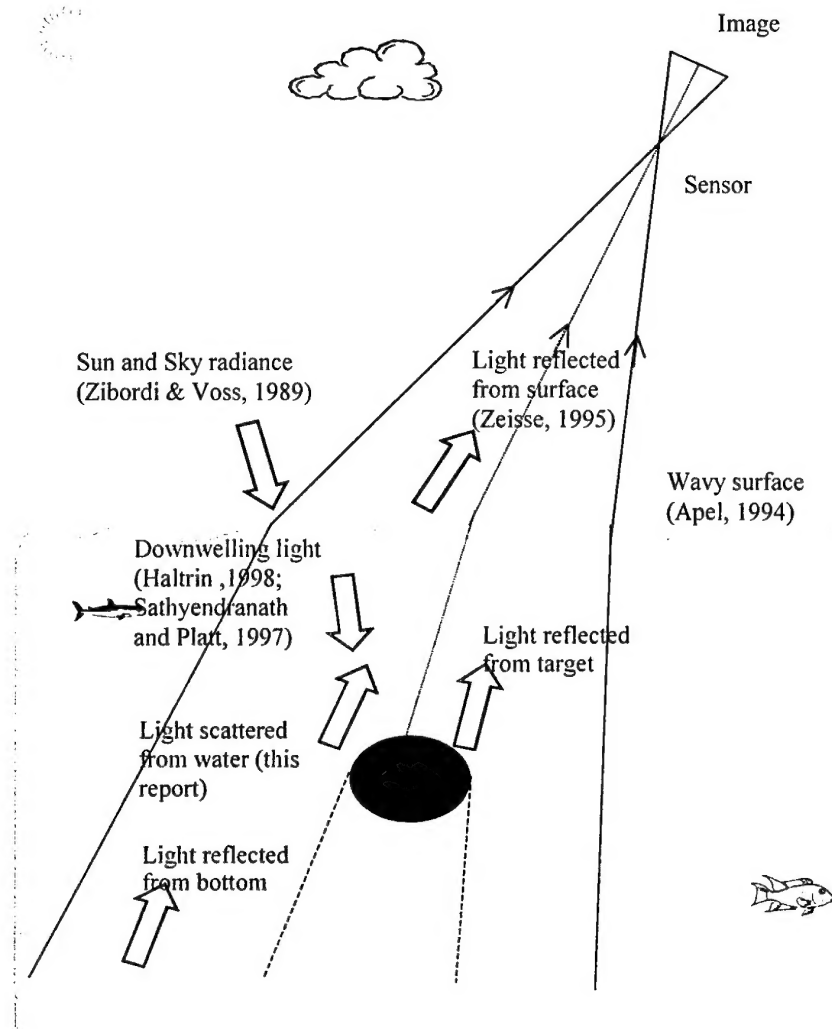


Figure 1. Passive sensor model features. The names of the authors indicate the models used.

2. Simulation Software Design

All model components have been programmed and implemented in the software simulating passive images of underwater objects. The skeleton of this software is the ray-tracing loop. All rays are independent of each other. They are generated one by one starting from the image plane of a sensor. Then their path is followed through atmosphere, sea surface and water, and radiance in the ray path is calculated at various parts of the ray using the corresponding models.

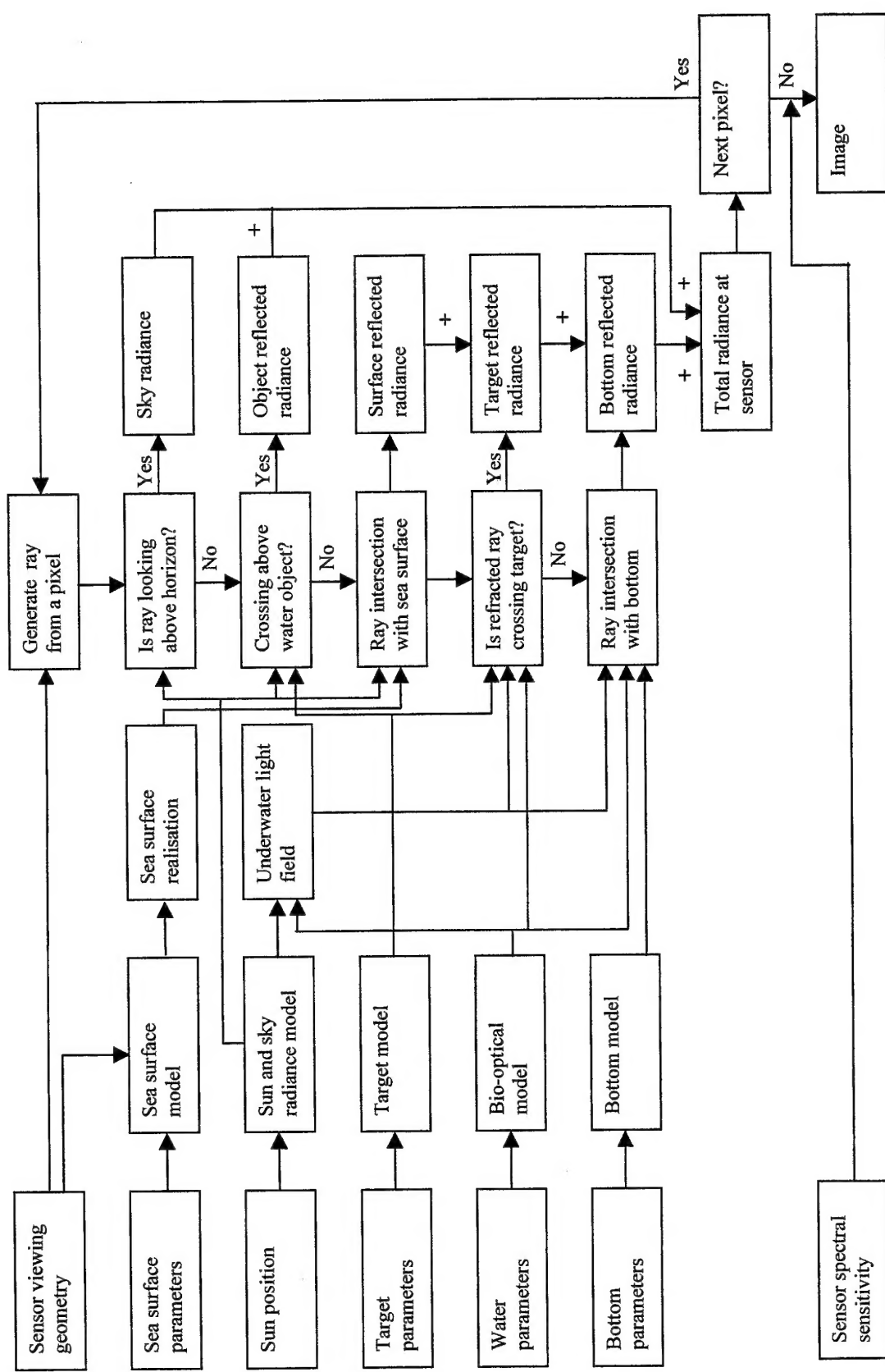


Figure 2. The simulation software flow chart.

The simulation software is written in C++ in platform independent way. It can be run on a personal computer or on a UNIX machine. The input parameters are provided as a text file that can be generated on a PC using a Graphical User Interface (GUI) developed specifically for this application.

The simulation software flow chart is presented in Figure 2. At the beginning of the ray-tracing loop a ray is generated from a pixel in the image plane using input parameters for the sensor viewing geometry. Then the program determines whether this ray is looking above horizon and, if this is true, calculates radiance into the ray from the direction of sky pointed by the ray using the sun and sky radiance model. This radiance is the only contribution to the total radiance field at the sensor and we go to the next pixel to generate a new ray.

If the ray direction is below horizon, we determine next whether it crosses the above water part of the object, if there is any. If this is the case, the program calculates radiance reflected from the above water part of the target using the sun and sky model and the target shape and reflectivity parameters. Again, this is the end of this ray and we go on to the next pixel.

If the target is completely underwater or this specific ray does not intersect the target surface, we need to find the ray intersection with the sea surface using the sea surface realisation. From the latter we also find the wave facet slopes and the surface elevation at the point of intersection. Variances of capillary wave slope distribution are calculated from the sea surface model. This information is used to calculate the sun and sky radiance reflected from the sea surface. This radiance is added up to the total radiance at the sensor and the ray is followed further through the sea surface. The wave slopes calculated from the sea surface realisation are used to calculate the direction of the refracted ray.

The program then determines whether the refracted ray crosses the underwater object. If it does, the radiance reflected from the target surface is calculated using the model for the underwater light field. The reflected radiance is then transferred through the water taking into account the model for light attenuation by water. It is then transmitted through the water surface and added up to the total radiance at the receiver.

If the ray does not cross the target, it is followed to the bottom. The radiance reflected from the bottom is calculated and treated in similar way to that reflected from an underwater object. It is added up to the total radiance at the sensor, and the program goes on to the next pixel.

Once the loop through all the pixels is finished, the total radiance at the receiver is convolved with sensor spectral sensitivity to produce an image.

3. Sun and Sky Radiance Model

To simulate the image of an underwater object we need a reasonably accurate model of the light field illuminating the object. For passive sensors such illumination originates from direct sun light and light scattered by the atmosphere. Therefore, we need a model of spectral sun and sky radiance at sea level. MODTRAN is widely used in the scientific community for such calculations and probably represents the most accurate and universal model of sun and sky radiance. However, it is time consuming and it is worth having a simpler model, which may describe a limited range of atmospheric conditions but is sufficiently accurate and robust.

One such simple model is described by Zibordi and Voss (1989). The model is based on an approximate solution of the radiative transfer equation for a plane parallel, homogeneous, cloudless atmosphere bounded by a lambertian surface. Zibordi and Voss (1989) compared the model with measurements performed for different wavelengths and solar zenith angles and found that agreement in most cases is within $\pm 10\%$. A detailed description of the sky radiance model can be found in Appendix A, which mainly reproduces the description from the paper of Zibordi and Voss (1989) and is given here for completeness.

We compared this model with MODTRAN calculations. A rigorous comparison would require many time consuming MODTRAN computations and we leave such an exercise for future work. Here we make comparison at selected parameters. The following figures show direct and diffuse solar irradiance at a horizontal surface and sky radiance at several viewing angles. For all computations the sun zenith angle was 45 degrees. The Zibordi and Voss model includes the following parameters: Angstrom parameters for aerosol optical thickness $\alpha_0 = 0.05$, $\beta = 0.8$, the asymmetry parameters for the two term Henyey-Greenstein (TTHG) function $a=0.962$, $g_1=0.713$, and $g_2=0.759$, ozone concentration $C_{O_3} = 0.33$ cm and water vapour concentration $C_w = 2.5$ cm. It was found by Zibordi and Voss that these parameters most accurately describe their experimental results. The field experiment was conducted on fine day of 15 May on California coast. In the MODTRAN calculations we used default parameters for the midlatitude summer model with navy maritime aerosol model for open ocean. From our point of view this represents the closest to the conditions of experiment default model. Three sets of calculations were performed with the single scattering option, the two-flow multiple scattering (MS) model, and the DISORT model for multiple scattering with sixteen streams.

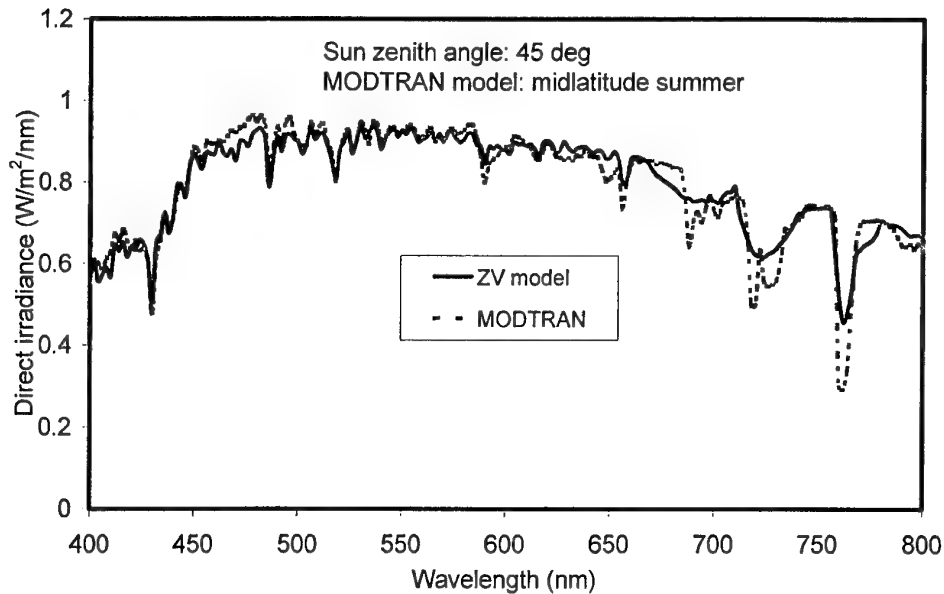


Figure 3. Direct irradiance at horizontal surface. Sun zenith angle is 45 degrees.

Figure 3 compares direct irradiance at the horizontal surface using the two approaches. Reasonably good agreement can be seen in the visual part of the spectrum with most disagreement in the near infrared part of the spectrum, which is not of much significance for underwater studies.

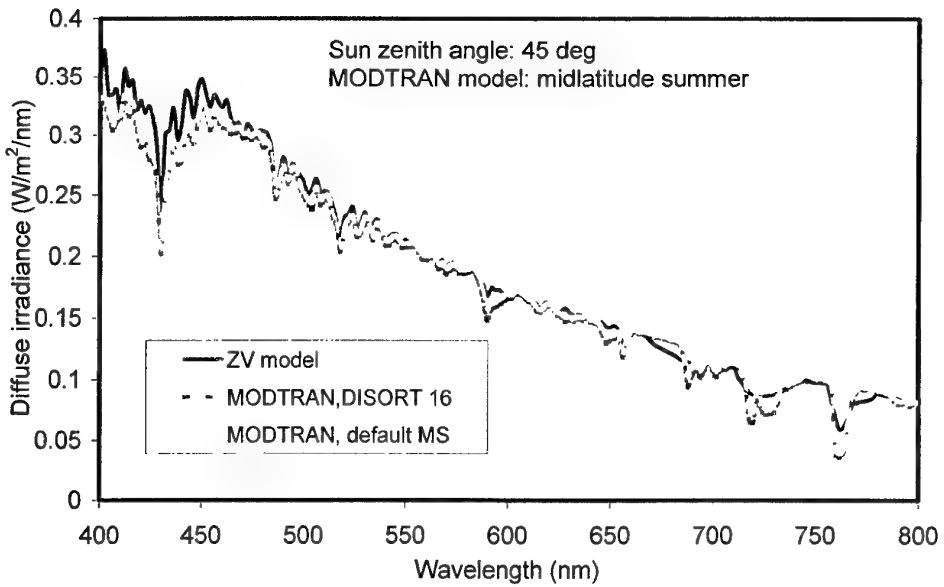


Figure 4. Diffuse irradiance at horizontal surface. Sun zenith angle is 45 degrees.

Figure 4 shows relatively good agreement between MODTRAN and the Zibordi and Voss model for diffuse irradiance at horizontal surface with the latter model giving higher values in blue part of the spectrum.

Figures 5 to 7 show sky radiance at various viewing angles. The main conclusion from these figures is that the single scattering approximation in MODTRAN gives quite poor results. Even the default two-stream multiple scattering approximation is not as good as the DISORT option with 16 streams. Thus, if we need to take into account sky radiance very accurately, we will need to use the DISORT option in MODTRAN with at least 16 streams, which will increase calculation time dramatically. The computation time of one viewing direction for a Pentium II 500MHz computer was 1 min 45 sec for single scattering mode, 2 min 33 sec for the default two-stream multiple scattering option, and about 90 min for the DISORT option with 16 streams. To represent radiance all over the sky accurately we need about 200 viewing angles. This equates to about 300 hours of MODTRAN computations for one atmospheric scenario. By atmospheric scenario we mean a single value of sun elevation angle above horizon for a given cloud cover, aerosol model etc. Precomputed sky radiance can be easily rotated by any azimuthal angle, so the sun azimuth could be set to zero during preliminary computation of the sky radiance. We should note here, however, that if the cloud cover is not isotropic, it will be fixed with respect to the sun position, so sun and sky can be rotated as a whole around the sensor.

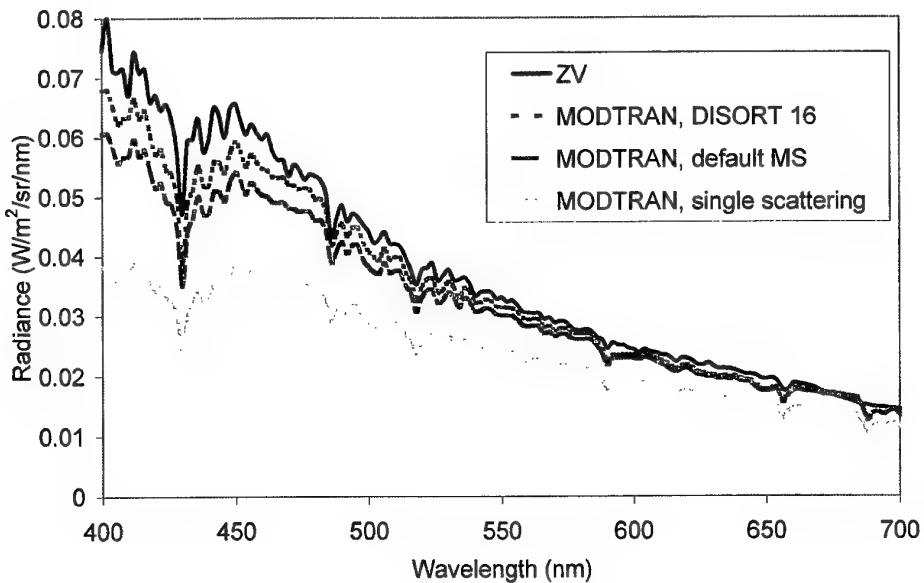


Figure 5. Sky radiance. Sun zenith angle is 45 degrees, viewing zenith angle is 5 degrees, and viewing azimuth is 180 degrees from the direction to the sun.

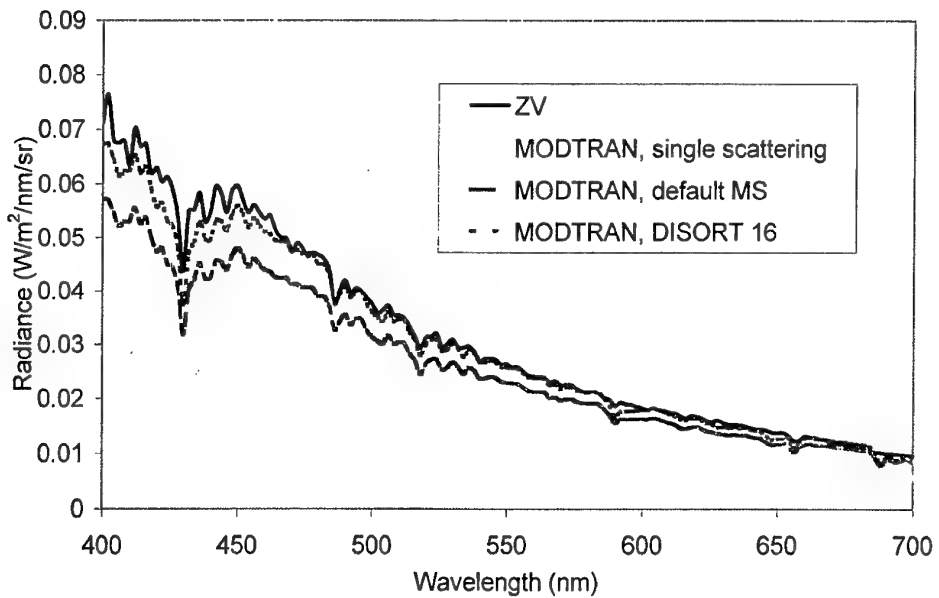


Figure 6. Sky radiance. Sun zenith angle is 45 degrees, viewing zenith angle is 45 degrees, and viewing azimuth is 180 degrees from the direction to the sun.

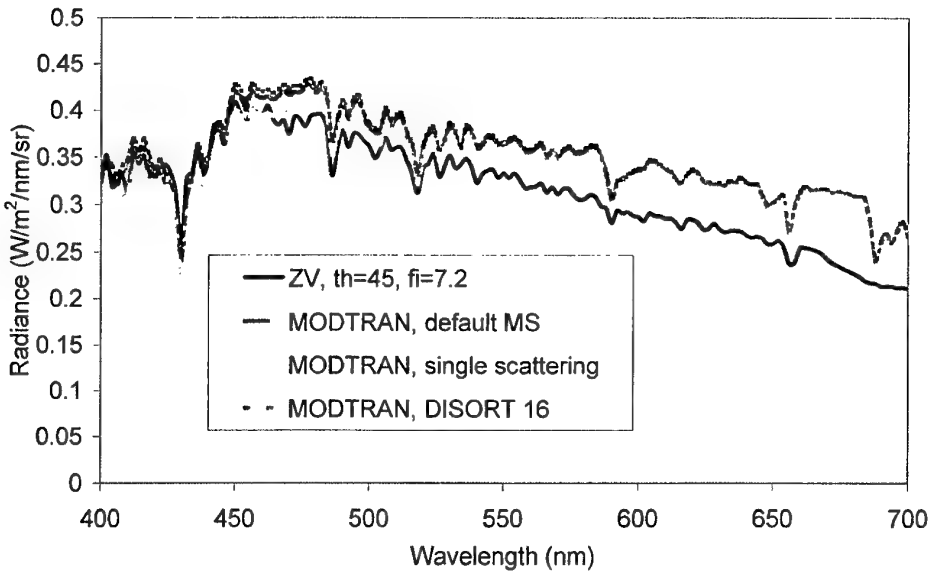


Figure 7. Sky radiance. Sun zenith angle is 45 degrees, viewing zenith angle is 45 degrees, viewing azimuth is 7.2 degrees from the direction to the sun.

4. Sea Surface Model

The sea surface is modelled in the following form (Massel, 1996):

$$\eta(x, y, t) = \sum_{m=1}^M \sum_{n=1}^N a_{mn} \cos(k_m x \cos \theta_n + k_m y \sin \theta_n - \omega_m t + \phi_{mn}) \quad (4.1)$$

Here a_{mn} is the amplitude of individual waves, k_m is the wavenumber, ω_m is the wave frequency, and ϕ_{mn} is the phase of individual waves. M and N are the number of intervals in the wavenumber and azimuth θ , respectively.

Coefficients in equation (4.1) are calculated from a wave spectrum using the following procedure. First we determine the range of wavelengths in the random realisation of the sea surface. The minimum wavelength is set to be twice the minimum pixel size at sea surface. The maximum wavelength is twice the maximum size of the whole field of view footprint at sea surface. The optical properties of the sea surface due to shorter waves are modelled statistically.

The wavenumber interval $[k_{\min}, k_{\max}]$, determined by the maximum and minimum wavelength, respectively, is divided into M intervals with middle points \hat{k}_m and interval sizes Δk_m . The wavenumber k_m is randomly chosen from each interval as $k_m = \hat{k}_m + (r - 0.5)\Delta k_m$, where r is a random number, $0 \leq r \leq 1$. The direction of a mode propagation is chosen randomly as $\theta_n = \hat{\theta}_n + (r - 0.5)\Delta \theta_n$, $1 \leq n \leq N$. The phase of a mode is a random number in the interval $[0, 2\pi]$, $\phi_{mn} = 2\pi r$.

The amplitude of a mode a_{mn} is calculated from a wavenumber spectrum $\Psi(k, \theta)$ (Phillips, 1977):

$$a_{mn} = \sqrt{\Psi(k_m, \theta_n) k_m \Delta k_m \Delta \theta_n} \quad (4.2)$$

The frequency of the mode is determined from the dispersion equation (LeBlond and Mysak, 1978):

$$\omega^2 = \left(gk + \frac{\sigma k^3}{\rho} \right) \tanh kH, \quad (4.3)$$

where g is the specific gravity, σ is the water surface tension, ρ is the water density, H is the water depth. For gravity waves in deep water, equation (4.3) can be approximated as follows:

$$\omega^2 = gk \quad (4.4)$$

This approximation is accurate for most of the applications of imaging through the water surface that we are concerned with in the present work.

Any wave-number spectrum can be used to generate a sea surface realisation. In our simulations we used the directional wave-number spectrum of Apel (1994) (Appendix B).

5. Radiance Reflected from Sea Surface

Reflection of sun and sky radiance from a wavy sea surface is modelled following the work of Zeisse (1995). In general terms the reflected radiance can be expressed by the following equation:

$$L_r = \iint_{\substack{\omega \leq \pi/2 \\ U_r = \text{const}}} \rho(\omega) L_s(\theta_s, \varphi_s) q(\theta_r, \varphi_r, \zeta_x, \zeta_y, W) d\zeta_x d\zeta_y \quad (5.1)$$

where $\rho(\omega)$ is the Fresnel reflection at the angle of incidence ω , θ_r, φ_r are the zenith and azimuth angles to the receiver, θ_s, φ_s are the zenith and azimuth angles of ray reflected from a wave facet towards sky, $L_s(\theta_s, \varphi_s)$ is the radiance from sky or sun, ζ_x, ζ_y are the slopes of a wave facet, $q(\theta_r, \varphi_r, \zeta_x, \zeta_y, W)$ is the interaction probability density (Plass *et al.*, 1975), and W is the wind speed. The latter can be expressed via the occurrence probability density and calculated using slope variances obtained from a surface wave spectrum for waves shorter than the pixel footprint size at the sea surface. The integral conditions indicate that the angles of incidence less than 90 degrees are considered and the direction to the receiver is kept constant during integration over possible wave slopes at the sea surface. In the case of reflection of the sun, equation (5.1) can be significantly simplified due to the small value of the solid angle subtended by the solar disk (see Zeisse, 1995 for details).

6. Radiance from below sea surface

The calculation of radiance scattered from water in the direction of the receiver along a ray path is illustrated in Figure 8. In the computation of radiance we make the following assumptions:

- we assume the single scattering approximation;
- the optical properties of seawater, both inherent and apparent, are uniform with depth;

- the volume scattering function of water is constant in the direction of backscattering;
- the mean cosine of the downwelling light stream is constant with depth.

These assumptions simplify the analysis significantly and are sufficiently accurate for initial estimation of system performance. Further improvement of the model is left for future work. This may require a numerical solution for the light field in water.

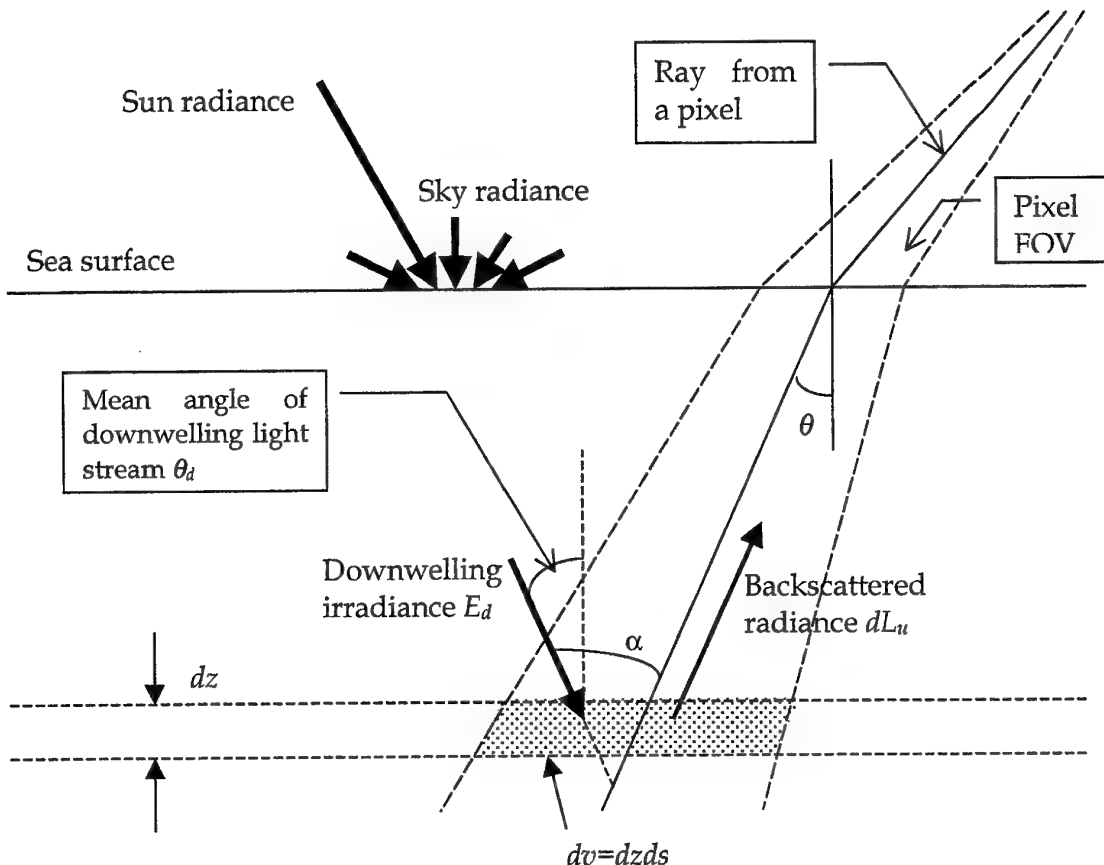


Figure 8. Calculation of radiance into individual pixel's field of view (FOV).

Intensity of light scattered in the direction of the receiver by the volume $dv = dz ds$ is by definition (Jerlov, 1976):

$$dI = \frac{E_d(z)}{\mu_d(z)} \beta(\alpha) dv \quad (6.1)$$

where $\beta(\alpha)$ is the volume scattering function of seawater, $E_d(z)$ is the downwelling irradiance at the depth z , $\mu_d(z) = \cos\theta_d$ is the mean cosine of the downwelling light stream at depth z , α is the angle between the mean direction of downwelling light and a ray, such that:

$$\cos\alpha = \cos\theta_d \cos\theta + \sin\theta_d \sin\theta \cos\varphi, \quad (6.2)$$

where φ is the azimuth angle between the direction to receiver and downwelling light field.

After some transformations we find that radiance scattered from the volume element into an individual pixel's field of view (FOV) just below the sea surface is

$$dL_u(0^-) = \frac{E_d(0^-)}{\mu_d \cos\theta} \beta(\alpha) \exp\left[-\left(K_d + \frac{K_L}{\cos\theta}\right)z\right] dz \quad (6.3)$$

Here we assume that the radiance attenuation coefficient K_L , the mean cosine of the downwelling light μ_d and the attenuation coefficient of the downwelling irradiance K_d is constant with depth, so the downwelling irradiance at depth z is

$$E_d(z) = E_d(0^-) \exp(-K_d z), \quad (6.4)$$

where $E_d(0^-)$ is the downwelling sun and sky irradiance just below the sea surface.

The radiance reflected from water along the whole ray path is

$$L_u(0^-) = \int_0^z dL_u(0^-) dz \quad (6.5)$$

We assume here that the volume scattering function is constant in the direction of backscattering, i.e. for $\pi/2 \leq \alpha \leq \pi$ $\beta(\alpha) = \frac{b_b}{2\pi}$, where $b_b = 2\pi \int_{\pi/2}^{\pi} \beta(\alpha) \sin\alpha d\alpha$ is the backscattering coefficient. This is a normal assumption in an analytical approach to radiative transfer in seawater based on a characteristic, highly forward peaked, volume scattering function of seawater (Zege, 1991). Assuming also that μ_d is constant with depth we have the following equation for the radiance just below the sea surface in an individual pixel's FOV

$$L_u(0^-) = \frac{E_d(0^-)b_b}{2\pi\mu_d} \frac{1}{K_d \cos\theta + K_L} \left[1 - \exp\left(-\left(K_d + \frac{K_L}{\cos\theta}\right)z\right) \right] \quad (6.6)$$

The radiance just above the sea surface is (Jerlov, 1976)

$$L_u(0^-) = \frac{L_u(0^-)(1 - \rho_{wa})}{n^2}, \quad (6.7)$$

where n is the refractive index of sea water relative to air, and ρ_{wa} is the reflection coefficient for radiance coming from water to air.

The irradiance just below the air-water interface, $E_d(0^-)$, is the sum of the direct sun irradiance, $E_d^{sun}(0^-)$, and the diffuse irradiance from the sky, $E_d^{sky}(0^-)$:

$$E_d(0^-) = E_d^{sun}(0^-) + E_d^{sky}(0^-) \quad (6.8)$$

Following Diersen and Smith (1997) we calculate the irradiances just below the sea surface according to the following approximate equations:

$$E_d^{sun}(0^-) \approx 1.03(1 - \rho_{sun}(\theta_s))E_d^{sun}(0^+), \quad (6.9)$$

where ρ_{sun} is Fresnel reflectance of direct radiance from the sun.

$$E_d^{sky}(0^-) \approx 0.962E_d^{sky}(0^+). \quad (6.10)$$

Here $E_d^{sun}(0^+)$ and $E_d^{sky}(0^+)$ are the irradiances just above the sea surface of sun and sky, respectively.

To use equation (6.6) we need to calculate the apparent optical properties of water, K_d and μ_d , from the inherent optical properties of water. Several approximations are available for these parameters in the literature. Sathyendranath and Platt (1997) give the following equation for the attenuation coefficient of downwelling irradiance:

$$K_d = \frac{a + b_b}{\mu_d}, \quad (6.11)$$

where a is the absorption coefficient of water.

This equation requires knowledge of the mean cosine of the downwelling light stream μ_d . In the near sea surface region, under direct solar illumination, this parameter can be approximated by the cosine of the refracted solar zenith angle, μ_{sw} :

$$\mu_{sw} = \cos \left[\sin^{-1} \left(\frac{1}{n} \sin \theta_s \right) \right], \quad (6.12)$$

where θ_s is the sun's zenith angle. Another extreme approximation for μ_d is its asymptotic value in sea depth (Haltrin, 1998):

$$\mu_d = \frac{1}{2 - \bar{\mu}}, \quad (6.13)$$

where $\bar{\mu}$ is the average cosine over the deep water angular distribution of radiance (Haltrin, 1998):

$$\bar{\mu} = \left\{ \frac{a}{a + 3b_b + [b_b(4a + 9b_b)]^{1/2}} \right\}^{1/2}. \quad (6.14)$$

Another useful approximation for K_d is given by Kirk (1984):

$$K_d = \frac{a}{\mu_{sw}} \left[1 + (0.425\mu_{sw} - 0.19) \frac{b}{a} \right]^{1/2}, \quad (6.15)$$

where b is the scattering coefficient of water. This approximation is based on numerical simulations using the Petzold turbid-harbour phase function. Kirk (1991) also extended the approximation to other scattering functions:

$$K_d = \frac{a}{\mu_{sw}} \left[1 + G(\mu_{sw}, g) \frac{b}{a} \right]^{1/2}, \quad (6.16)$$

where

$$G(\mu_{sw}, g) = \mu_{sw} \left(\frac{2.236}{g} - 2.447 \right) - \left(\frac{0.849}{g} - 0.739 \right). \quad (6.17)$$

Here g is the asymmetry parameter of the scattering phase function.

Comparison between different approximations for the attenuation coefficient of downwelling irradiance, K_d , is shown in Figure 9. The inherent optical properties were computed using the one-parameter bio-optical model (Section 7) with concentration of chlorophyll $C_c=1 \text{ mg/m}^3$ that is found to be a typical value for Australian coastal water (Section 7). Sun zenith angle is 60 deg. The asymmetry parameter of the scattering phase function $g=0.95$, which is characteristic value for seawater (Zeege, 1991).

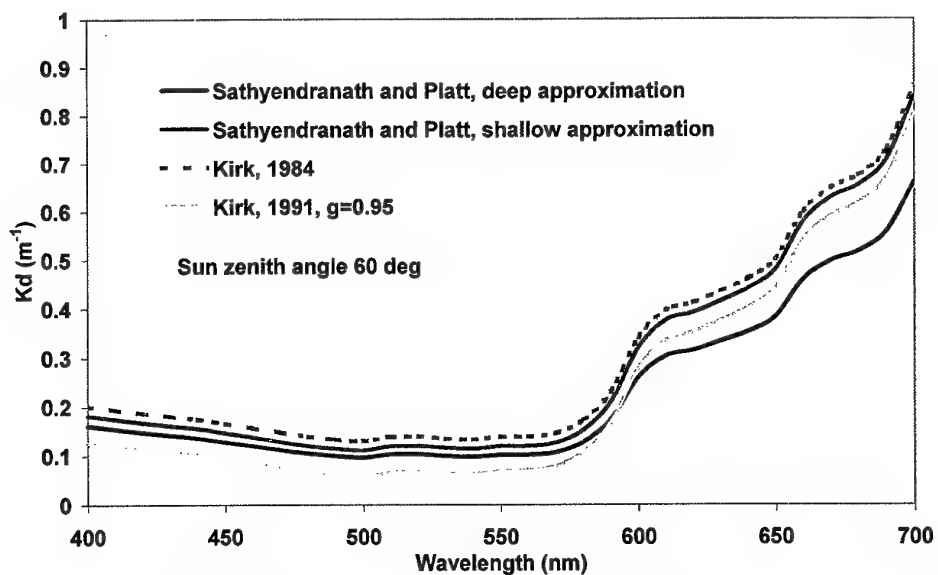


Figure 9. Comparison between different approximations for the attenuation coefficient of downwelling irradiance. Sun zenith angle $\theta_s = 60 \text{ deg}$. Phase function asymmetry parameter $g=0.95$.

For the radiance attenuation coefficient we use the following expression (Preisendorfer, 1976):

$$K_L = D_L(a + b_b), \quad (6.18)$$

where D_L is the distribution function. In the current work we assume that $D_L \approx 1$. This means that light propagating towards the receiver is lost only due to absorption and backscattering. Such an approximation may only be applied for light reflected from an element of the water column. For light reflected from a target one should use the total attenuation coefficient as K_L .

A more accurate approximation for D_L is given by Lee *et al.* (1998):

$$D_L \approx 1.2(1 + 2.0u)^{0.5}, \quad (6.19)$$

where

$$u = b_b / (a + b_b), \quad (6.20)$$

Equation (6.19) was obtained by fitting an analytical model for the remote sensing reflection to that calculated by Hydrolight (Mobley, 1994). In further improved versions of the simulation software we will use either more accurate approximation (6.19) or full numerical solution for the radiance field by the Hydrolight. An investigation in feasibility of combining the Hydrolight package with the image simulation software is currently being conducted.

The remote sensing reflection is defined as the ratio of upwelling radiance to downwelling irradiance evaluated just below the sea surface:

$$r_{rs} = L_u(0^-) / E_d(0^-). \quad (6.21)$$

From equation (6.6) for the down-looking sensor ($\theta = 0$) and deep water we have:

$$r_{rs}^{dp} = \frac{u}{2\pi(1 + \mu_d D_L)}. \quad (6.22)$$

Figure 10 compares equation (6.22) with values r_{rs}^{dp} determined by other approximations obtained from numerical calculations. Morel and Gentili (1993) give the following expression for the remote sensing reflectance:

$$r_{rs}^{dp} \approx \frac{0.0922}{1-u} u. \quad (6.23)$$

Lee *et al.* (1998) found the following approximation from the Hydrolight calculations:

$$r_{rs}^{dp} \approx (0.070 + 0.155u^{0.752})u \quad (6.24)$$

One can see from the figure that equation (6.22) agrees with other approximations only for low values of u which correspond to open ocean water. It follows from one parameter bio-optical model (Section 7) that the values of the parameter u for most waters are less than 0.05 (Figure 11). Thus the approximation of (6.22) is mostly useful.

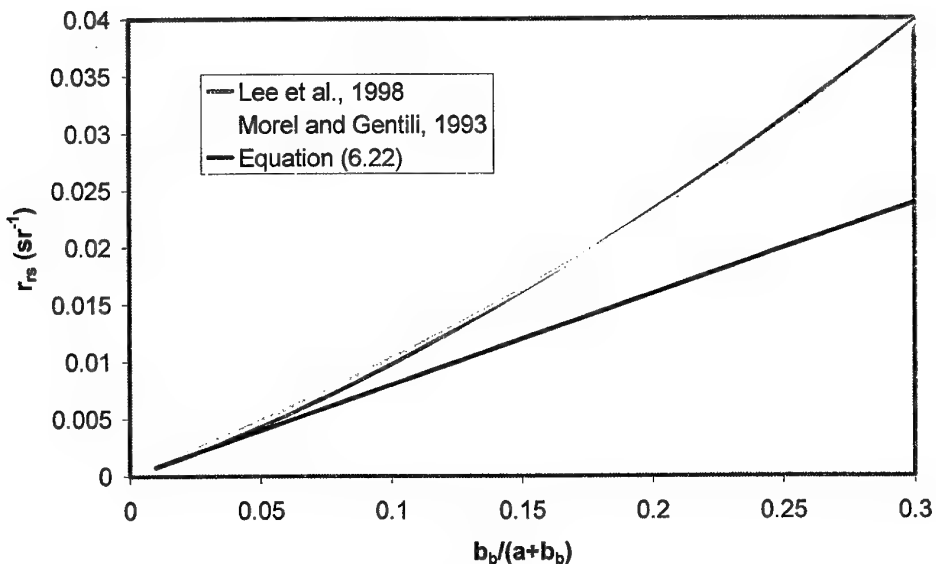


Figure 10. Comparison of r_{rs}^{dp} values as determined by different approximations.

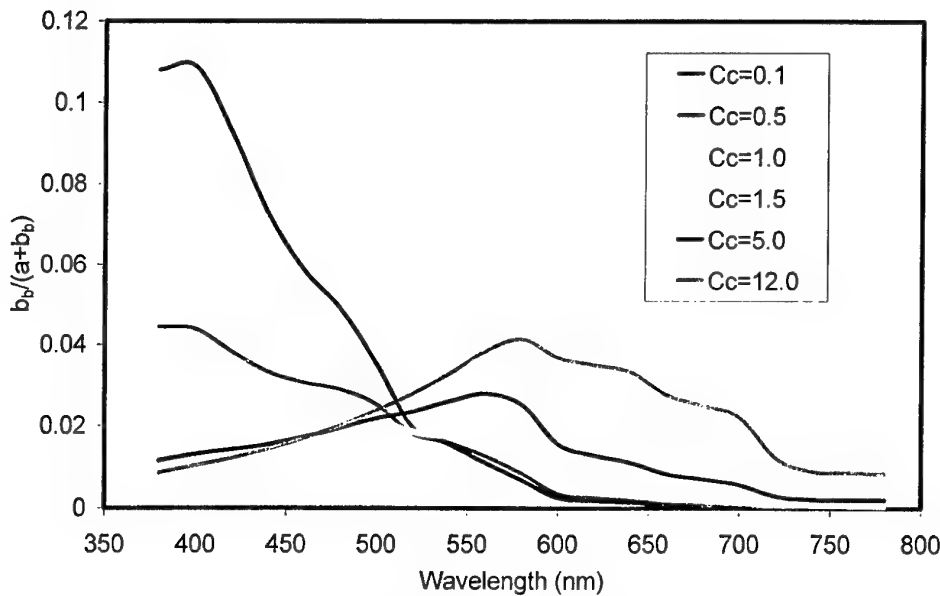


Figure 11. Values of parameter $u = b_b / (a + b_b)$ versus wavelength for different concentrations of chlorophyll (mg/m³).

7. Bio-Optical Model

A bio-optical model relates the optical properties of ocean water to concentrations of its biological components such as chlorophyll and Dissolved Organic Matter (DOM). The model used in our simulations is the one described by Haltrin (1998), that summarises empirical data accumulated by many researchers, mainly for open ocean water. For completeness, we reproduce equations from his paper in Appendix C.

Here we compare the above model with experimentally measured values of absorption and total attenuation coefficient. The measurements were taken using a WetLabs AC-9 spectral transmissometer at several different locations in Australian coastal waters. First we consider how well the one-parameter model fits the measured data. The fitting was performed by minimising the sum of squares of the relative error between the model and measured values:

$$S(C_c) = \sum_{i=1}^{i=9} \left\{ \left(\frac{a(\lambda) - a_i}{a_i} \right)^2 + \left(\frac{c(\lambda) - c_i}{c_i} \right)^2 \right\} \quad (7.1)$$

For the one-parameter model this sum is a function of only the concentration of chlorophyll that can be found from minimisation procedure. All other concentrations, i.e. the concentration of humic and fulvic acids, small and large particles, are derived

from the concentration of chlorophyll due to correlation relations between those concentrations (see Appendix C).

Figure 12 shows one example of measured data. Here the absorption (labelled as $a + \text{wavelength}$) and total attenuation coefficients (labelled as $c + \text{wavelength}$) measured in Sydney Harbour on 31 of August 2000 are shown. We can see a characteristic near-bottom layer of higher turbidity. Having applied the minimisation procedure at each depth, we obtain the following profiles of concentrations of various components of the water (Figure 13)

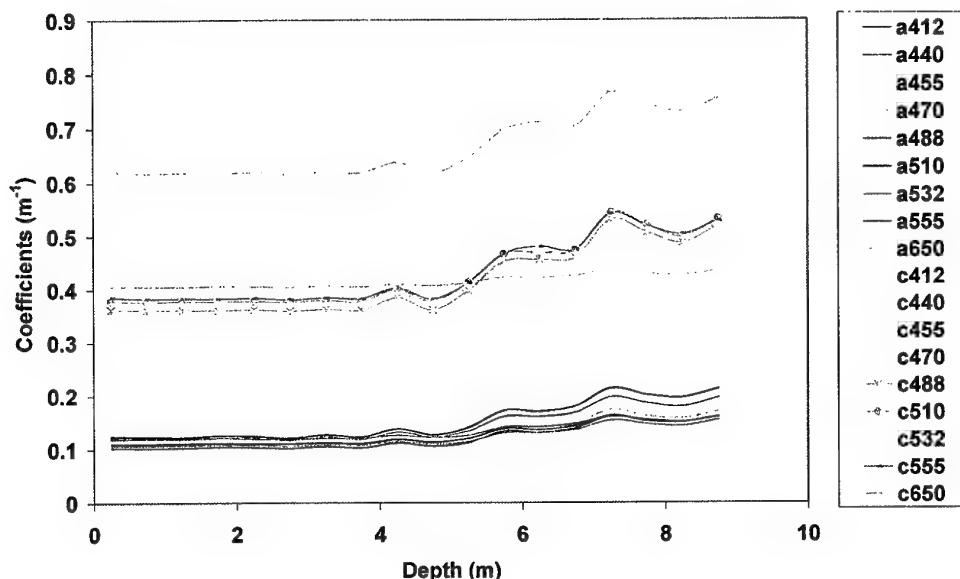


Figure 12. Absorption and total attenuation coefficients versus depth measured in Sydney Harbour.

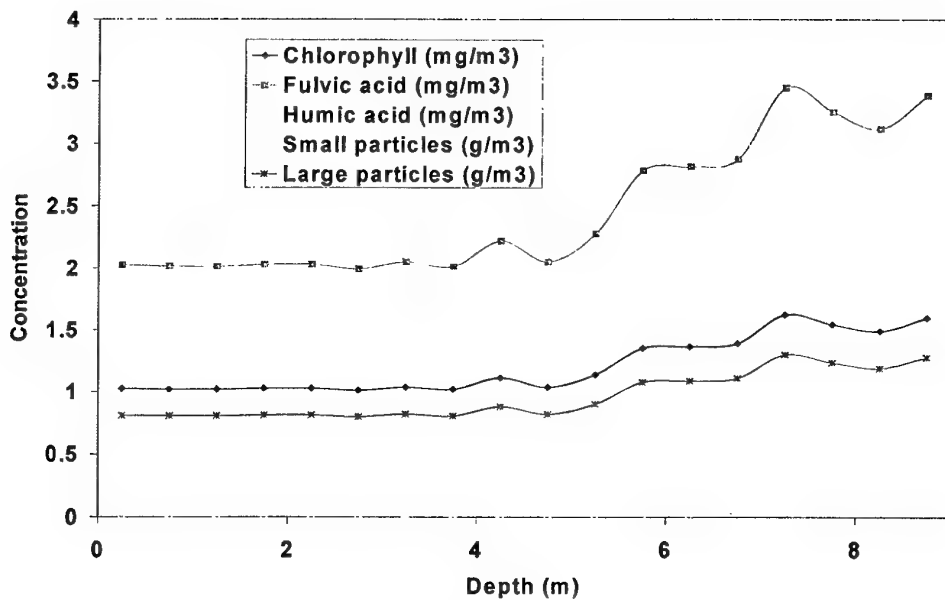


Figure 13. Concentrations of water components derived from measured absorption and total attenuation coefficients using the one-parameter model.

An example of model fit to the measured data at a particular depth is shown in Figure 14. We can see that this particular data from Sydney Harbour water can be described reasonably well by the one-parameter model. The maximum error is 18% for the absorption value at 555 nm. The fit of data from other sites in Sydney Harbour produced similar results with slightly higher maximum error, with up to 30% for some absorption values.

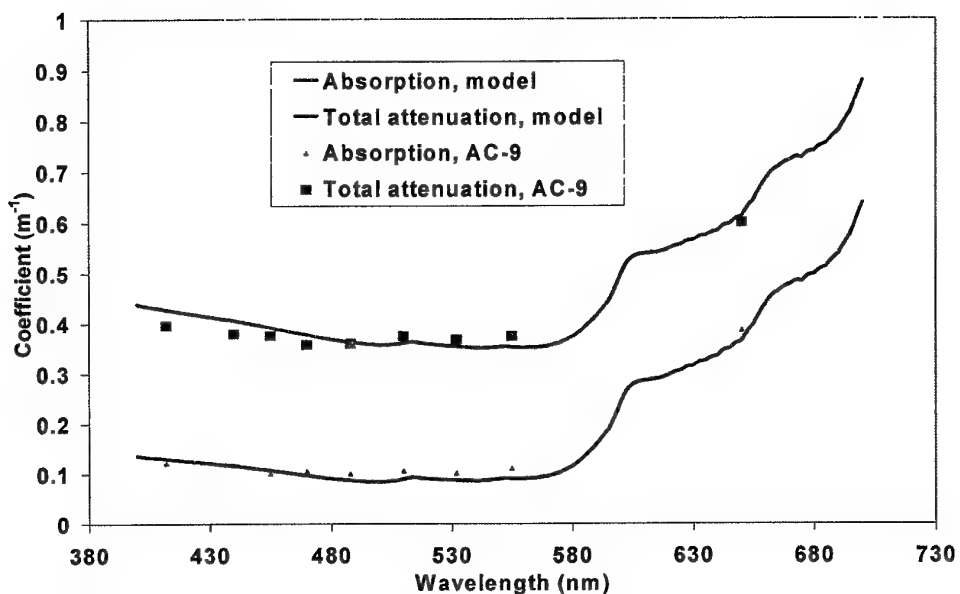


Figure 14. Comparison between the measured data and the one-parameter model for Sydney Harbour water at depth of 1.25 m. The concentration of chlorophyll obtained from minimisation of (7.1) is 1.02 mg/m³.

However, the data from other Australian coastal waters are not very well described by the one-parameter model. The following two graphs show the comparison between the model and the data measured in coastal water between Cairns and Thursday Island (Figure 15) and Cowley Beach (Figure 16). One can see that the model fit is not very good with errors up to 45% for absorption values at 555 nm. We can see that the concentration of chlorophyll derived from the data using the one-parameter model is higher for these waters. Poor fit of the measured data by the one-parameter model suggests that there is no strong correlation between concentrations of various components in analysed coastal water.

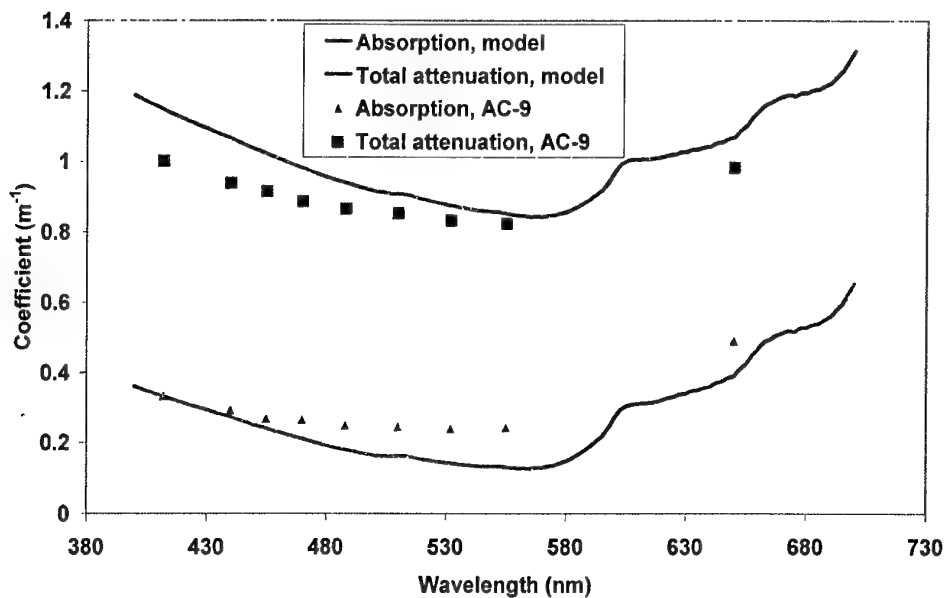


Figure 15. Comparison between the measured data and the one-parameter model for water between Cairns and Thursday Island at depth of 15 m. The concentration of chlorophyll obtained from minimisation of (7.1) is 2.65 mg/m³.

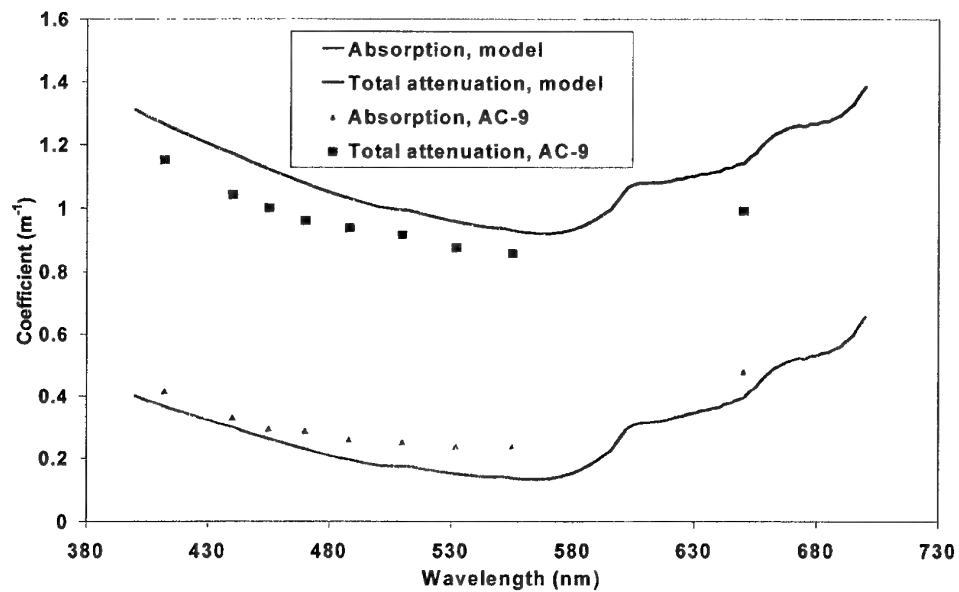


Figure 16. Comparison between the measured data and the one-parameter model for water at Cowley Beach at depth of 1.05 m. The concentration of chlorophyll obtained from minimisation of (7.1) is 2.89 mg/m³.

The following analysis shows that in some cases good fit still can be achieved with the equations in Appendix C but at the cost of increasing the number of independent parameters.

Here we consider the data measured near Kangaroo Island, South Australia ($35^{\circ}39'S$ and $136^{\circ}00'E$) on 31 January 2000 between 17:10 and 18:15 local time at depths of 5, 10, and 15 metres.

First, we will try to find the concentration of chlorophyll which gives the best fit to the experimental data using the least squares method as for above figures. Figure 17 shows the results of such fitting attempts. The fit is not very good with the model giving much lower values of scattering coefficient, the difference between total attenuation and absorption, than measured.

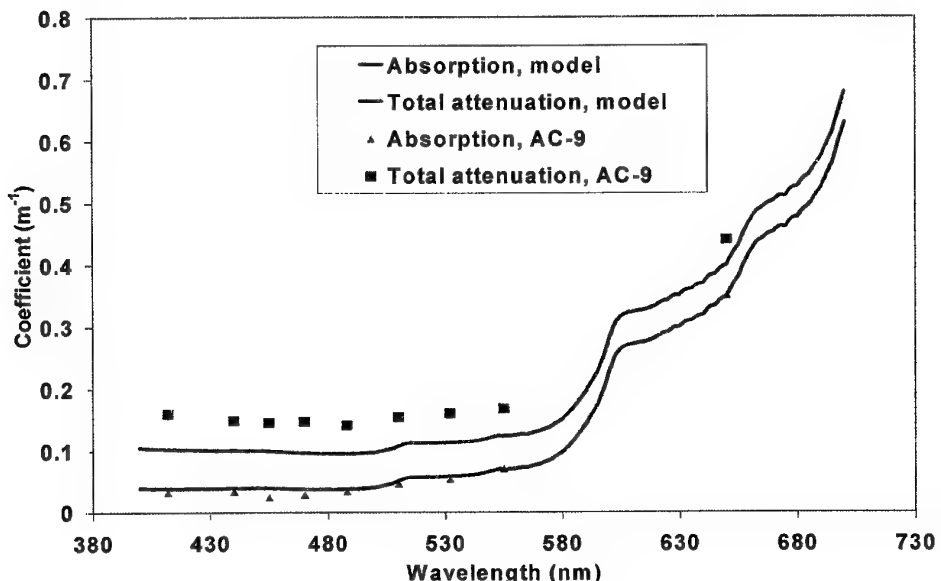


Figure 17. Comparison between the measured data and the one-parameter model for water off Kangaroo Island at depth of 5 m. The concentration of chlorophyll obtained from minimisation of (7.1) is 0.212 mg/m^3 .

To achieve a better fit of both coefficients we need to use more than one independent parameter. For this purpose we suggest using experimental values of absorption coefficient and equations (C.1), (C.8), and (C.9) to find the concentration of chlorophyll which gives the best fit of experimental data using equation (C.1). Then we assume the concentrations of small C_s and large C_l particles to be independent and find them by fitting experimental values of scattering coefficient by equation (C.2) using the least squares method. Using experimental values from 17:10 and depth of 5 m we find the following values of concentrations: $C_c=0.123 \text{ mg/m}^3$, $C_s=0.038 \text{ g/m}^3$, and $C_l=0.243 \text{ g/m}^3$. Figure 18 shows the results of this fitting procedure.

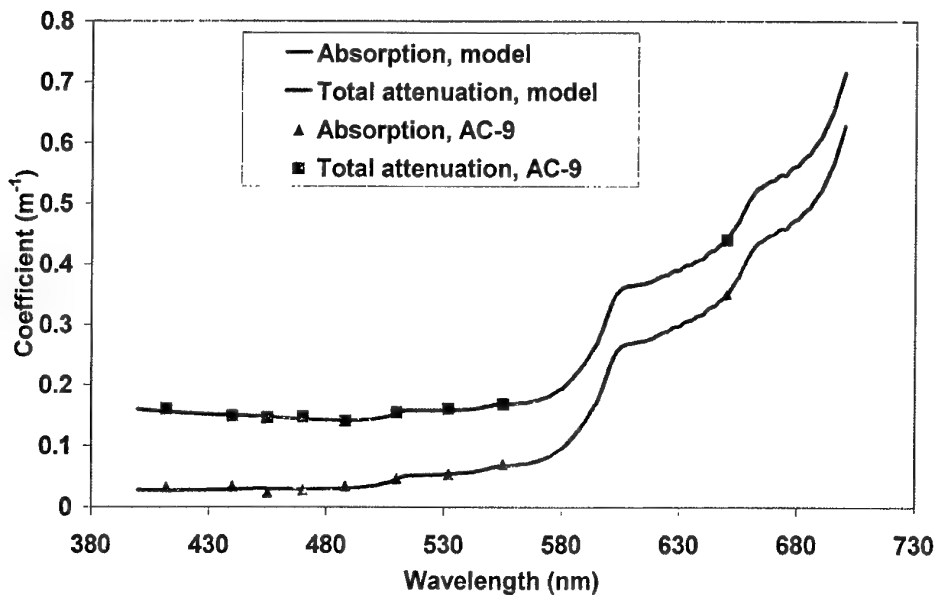


Figure 18. Three-parameter model fitting. $C_c=0.123 \text{ mg/m}^3$, $C_s=0.038 \text{ g/m}^3$, and $C_l=0.243 \text{ g/m}^3$.

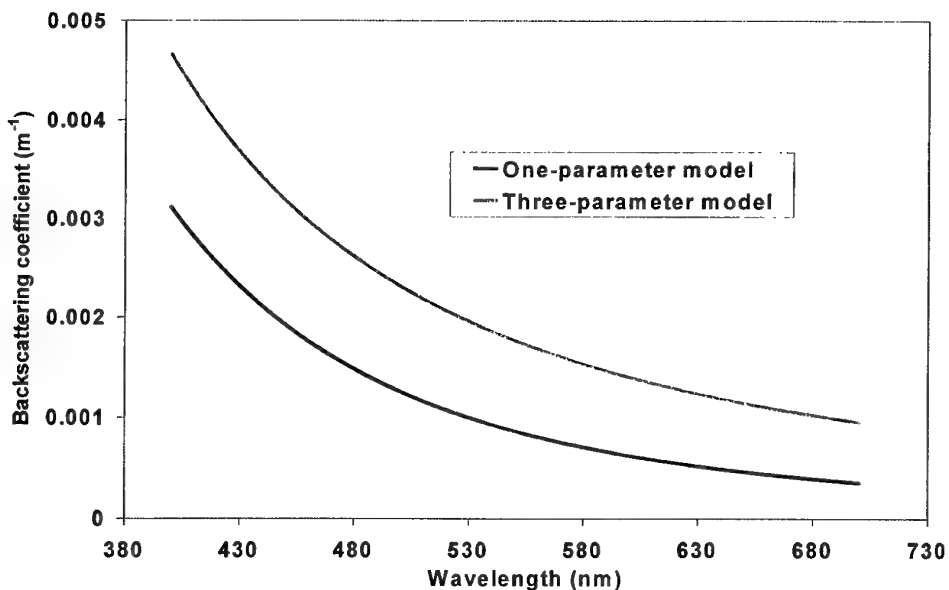


Figure 19. Backscattering coefficient. One-parameter model: $C_c=0.212 \text{ mg/m}^3$, $C_s=0.0038 \text{ g/m}^3$, and $C_l=0.163 \text{ g/m}^3$. Three-parameter model: $C_c=0.123 \text{ mg/m}^3$, $C_s=0.038 \text{ g/m}^3$, and $C_l=0.243 \text{ g/m}^3$.

Figure 19 shows that the backscattering coefficient for the three-parameter model is higher than for the one-parameter model. This is because the relative concentration

of small particles is higher for the three-parameter model than for the one-parameter model. The Kopelevich hydrosol parameter determines the relative volume of small particles and can be calculated as $C_s/(C_s + 2C_l)$. For the one-parameter model and for the data analysed, this parameter is 0.01 while for the three-parameter model the value of Kopelevich hydrosol parameter is 0.07, clearly indicating a higher relative concentration of the small particles. The asymmetry parameter of the Kopelevich phase function for the concentration of particles obtained from the one-parameter model is $g=0.953$. Concentrations of particles obtained from the three-parameter model give a value of asymmetry parameter of $g=0.934$. The Kopelevich phase function derived from the transmissometer data for water off Kangaroo Island using one and three-parameter model is presented in Figure 20.

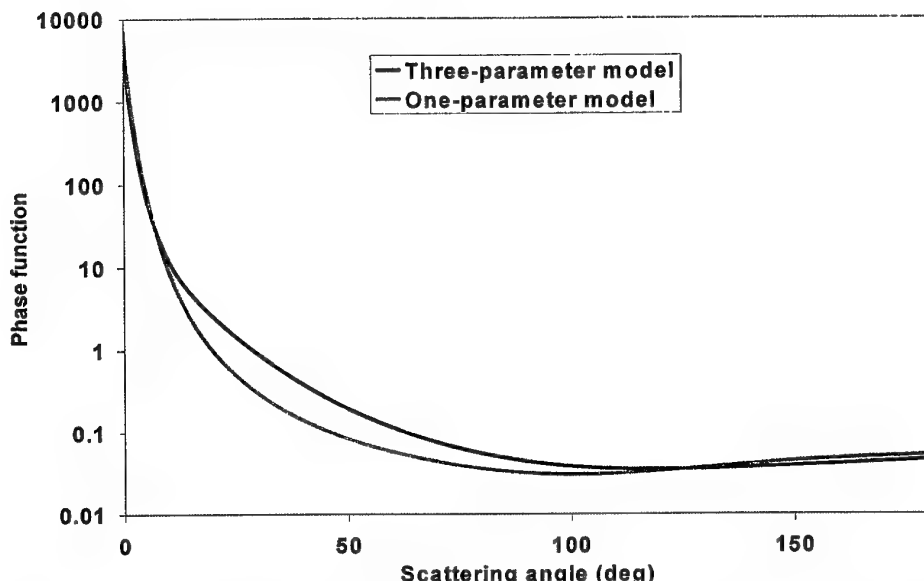


Figure 20. Kopelevich phase function derived from the AC-9 data for water off Kangaroo Island. One-parameter model: $C_c=0.212 \text{ mg/m}^3$, $C_s=0.0038 \text{ g/m}^3$, and $C_l=0.163 \text{ g/m}^3$, $g=0.953$. Three-parameter model: $C_c=0.123 \text{ mg/m}^3$, $C_s=0.038 \text{ g/m}^3$, and $C_l=0.243 \text{ g/m}^3$, $g=0.934$.

8. Target Rendering

Target rendering is based on the ray tracing technique. For each ray we determine whether it crosses the target surface. If it does, we find the coordinates of the intersection, illumination of the surface element, and reflected radiance towards the receiver.

A ray can be described by the following set of equations:

$$\begin{aligned} x &= x_0 + v_x t, \\ y &= y_0 + v_y t, \\ z &= z_0 + v_z t, \\ v_x^2 + v_y^2 + v_z^2 &= 1. \end{aligned} \tag{8.1}$$

For the ray in air (x_0, y_0, z_0) are the coordinates of the focal point of the camera. For the underwater part of the ray (x_0, y_0, z_0) are the coordinates of the ray intersection with the sea surface. Here v_x, v_y , and v_z are the directional cosines of the ray, t is the distance from the ray starting point to the current point (x, y, z) .

The target surface can be described as

$$F(x, y, z) = 0 \tag{8.2}$$

Substituting equation (8.1) into (8.2) we have an equation for the ray parameter t . For simple geometrical shapes such as spheres, cylinders, ellipsoids etc. this equation can be solved analytically. If the equation has multiple roots, we take the one with the minimum value of the parameter t . We can then find the unit vector \mathbf{n} normal to the target surface at the intersection point and calculate irradiance at the surface element:

$$E_n(\lambda) = \int_{2\pi} |(\mathbf{n} \cdot \mathbf{s})| L(\lambda, \mathbf{s}) d\Omega, \tag{8.3}$$

where $L(\mathbf{s})$ is the underwater radiance in the direction specified by the unit vector \mathbf{s} , $d\Omega$ is the differential solid angle. The integration in equation (8.3) is performed over the hemisphere outside the target.

We currently assume that the target surface is lambertian. Therefore, the radiance reflected towards the receiver will be

$$L_r(\lambda) = \frac{E_n(\lambda)}{\pi} R(\lambda), \tag{8.4}$$

where $R(\lambda)$ is the spectral reflectance of the target surface.

A complex three-dimensional target can be formed by combining several simple elements. In this case we need to solve the system of equations (8.1) and (8.2) for each

element of the target and take the solution with the minimum value of the ray parameter t . The sea bottom can be thought of as another element of the target. In most cases it will be an infinitely wide plane.

Target blur caused by light scattering in seawater is currently modelled using a simple empirical Point Spread Function (PSF) of ocean water (Voss, 1991). The PSF is applied in postprocessing to the 'underwater' part of the simulated image, i.e. to the radiance coming from below the sea surface. To do this we save separately the radiance from underwater $L_{mn}^{(uw)}$ and the radiance reflected from the sea surface $L_{mn}^{(ss)}$, where m and n are the pixel indices, and then convolve $L_{mn}^{(uw)}$ with the PSF:

$$\hat{L}_{mn}^{(uw)} = \sum_{m'=-r}^r \sum_{n'=-r}^r L_{m-m',n-n'} \text{PSF}(\tau_{m-m',n-n'}, \theta_{m-m',n-n'}^{m'n'}), \quad (8.5)$$

where τ_{mn} is the underwater path of the ray from pixel (m,n) , $\theta_{mn}^{m'n'}$ is the angle between underwater paths of the rays from pixels (m,n) and (m',n') :

$$\theta_{mn}^{m'n'} = \alpha \cos(v_x^{mn} v_x^{m-m',n-n'} + v_y^{mn} v_y^{m-m',n-n'} + v_z^{mn} v_z^{m-m',n-n'}), \quad (8.6)$$

where $(v_x^{mn}, v_y^{mn}, v_z^{mn})$ are the directional cosines of the underwater path of the ray from pixel (m,n) .

We can see from equations (8.5) and (8.6) that to perform such a convolution we need to also save the underwater paths and directional cosines for each ray. The convolution itself is rather a slow process. The use of the Modulation Transfer Function (MTF) and the Fast Fourier Transform (FFT) would increase the speed of this process significantly. However, the MTF is not suitable, for example, in the case of a three-dimensional target with a significant difference in range from the camera to different parts of the target. This is because the MTF technique does not allow variable blur across the image. In this case the use of PSF is preferable because PSF explicitly includes the range to the various points of the target through the ray optical path τ .

9. Sensor model

All of the above steps for calculating the radiance reflected or backscattered from various parts of the simulated scene eventually produce the spectral radiance arriving at the receiver. To simulate the image generated by a specific sensor we need to convolve the radiance at the receiver with the spectral sensitivity of the sensor.

In the case of the human eye or digital camera the spectrum must be transformed into three RGB values to produce an image:

$$L_r(\lambda) \otimes \begin{bmatrix} \bar{x}(\lambda) \\ \bar{y}(\lambda) \\ \bar{z}(\lambda) \end{bmatrix} \Rightarrow \begin{bmatrix} X \\ Y \\ Z \end{bmatrix} \Rightarrow \begin{bmatrix} R \\ G \\ B \end{bmatrix}, \quad (9.1)$$

where L_r is the radiance at the receiver, $\bar{x}, \bar{y}, \bar{z}$ are the colour-matching functions, X, Y, Z are the three standard primaries defined by International Commission of Illumination (CIE) in 1931, and the operator \otimes denotes convolution. The value Y also represents the luminance that will be used in the next section for comparison with the measurements.

In the case of a hyperspectral sensor there are several wavebands, each having a specific bandwidth. Average radiances within these wavebands can be calculated as follows:

$$L_r(\lambda) \otimes \begin{bmatrix} x_1(\lambda) \\ x_2(\lambda) \\ \dots \\ x_n(\lambda) \end{bmatrix} \Rightarrow \begin{bmatrix} \bar{L}_1 \\ \bar{L}_2 \\ \dots \\ \bar{L}_3 \end{bmatrix} \quad (9.2)$$

where $x_i(\lambda)$ is the spectral sensitivity function of bands.

10. Simulation Examples

Now we consider several examples of simulated images for different scenarios. Figure 21 shows a comparison of a simulated image (left) with a real photograph (right). The photograph was taken with a Nikon D1 digital camera in the Gulf of St Vincent on 20th of December 2000 at 11 a.m. Field of view of the camera lens was 51 degrees. The sun elevation above horizon was 59 degrees. The camera was pointed directly away from the sun. Estimated wind speed was about 5 m/s. The image on the left in Figure 21 is simulated for the same sun position with respect to the camera and the same field of view. Sea surface realisation is calculated for wind speed of 5 m/s using Apel's wave spectrum (Apel, 1994). Sky radiance is calculated from the model of Zibordi and Voss (1989).

The optical properties of seawater are calculated from the one-parameter bio-optical model of Haltrin (1998) with a concentration of chlorophyll value of 1.4 mg/m³. This

value is inferred from fitting the one-parameter model to the data measured on the day with the AC-9 spectral transmissometer.

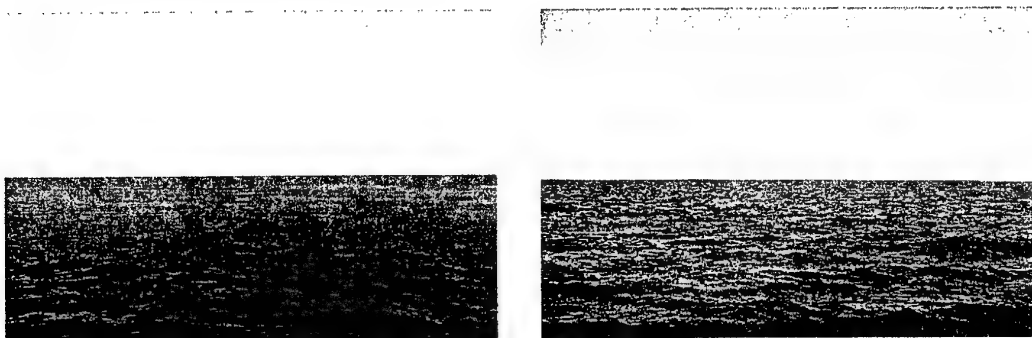


Figure 21. Comparison of simulated image (left) with real photograph (right).

Qualitatively, the simulated image compares reasonably well with the photograph especially in the sky area. The sea surface looks somewhat darker in the simulated image. One of the reasons for this may be as follows. The model always assumes the presence of small capillary waves in every pixel footprint at the sea surface. In reality, however, this may not be the case and some waves may be rather smooth on the scale of an individual pixel footprint. This may result in higher reflection of the sky radiance from the sea surface.

With respect to quantitative comparison, Figure 22 compares luminance calculated during the image simulation with the measurements made at the time of taking the photograph. The solid curve represents the luminance calculated for the vertical centre-line of the image with some extension beyond the upper boundary of the image. Zero angle in Figure 22 corresponds to the horizon with the negative angles representing atmosphere and the positive angles representing the sea surface. The measurements were made with a Tektronix LumaColor photometer J17 using luminance sensor-head J1803 with a field of view of 8 degrees. The sensor head was hand held during the measurements, so the look angle of the sensor and, therefore, position of the bars in Figure 22 is rather approximate. Taking this uncertainty into account, the calculated luminance compares reasonably well with the measured data.

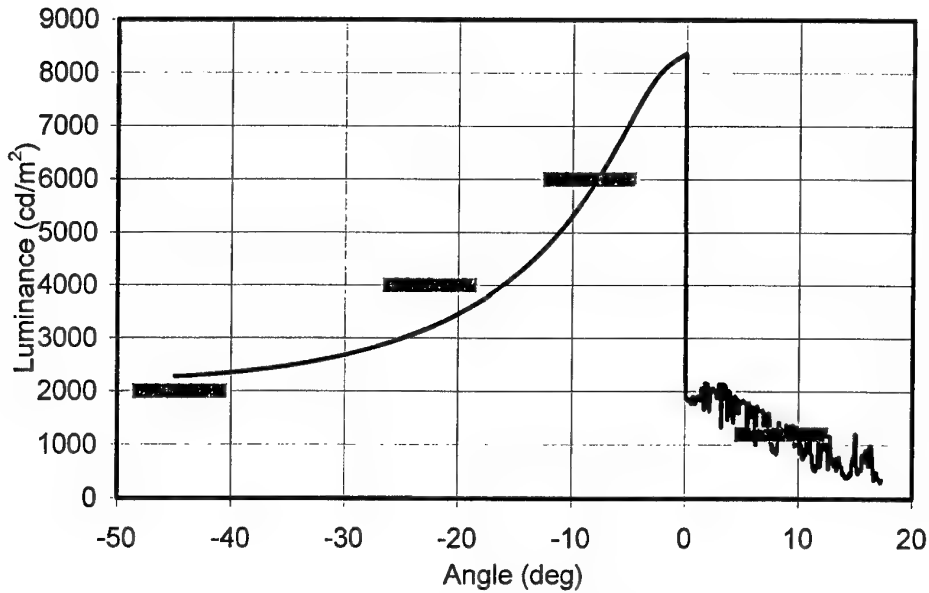


Figure 22. Comparison of simulated luminance (solid curve) with measurements (red bars). The width of red bars represents a field of view of 8 degrees.

Figure 23 demonstrates the model's capability to render three-dimensional underwater objects. In the simulated image we see a red cylindrical object, three grey spheres of various sizes, and a model of a Manta mine. The cylindrical object is composed of three basic geometrical objects: a cylinder and a disc at each end of the cylinder. The model of the Manta mine is composed of a red truncated cone with a red disc on top of the cone and a black disc on top of the red disc. The water depth is 2.5 m. The optical properties of water are calculated from the one-parameter model of Haltrin (1998) with a concentration of chlorophyll value of 1 mg/m³. The bottom is sand with reflectivity changing linearly from 40% at 400 nm to 55% at 700 nm. The image is disturbed by a wavy sea surface that is generated from Apel's wave spectrum using a wind speed value of 0.5 m/s. The wind direction is at 45 deg to the look direction. The sun elevation is 26 deg and its azimuth is 20 deg to the right from the look direction. The sensor height above sea surface is 5 m, zenith look angle is 30 degrees, and sensor field of view is 24 degrees. The blur due to scattering is modelled by applying the point-spread function to the underwater part of the image as described above in Section 8.

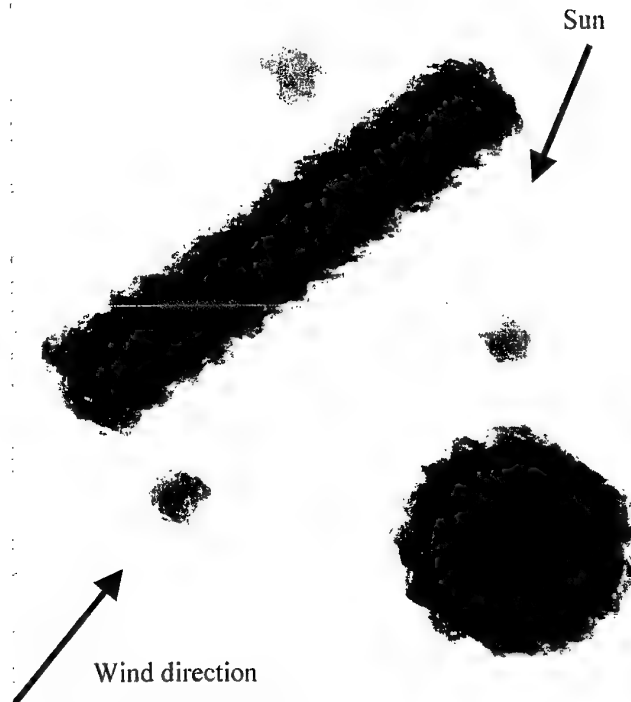


Figure 23. Simulated image of underwater objects.

Another passive system that can be simulated with our model is a hyperspectral sensor. Airborne hyperspectral sensors are predominantly "pushbroom" type sensors. In one swath the sensor takes an image of a narrow strip of water across the direction of aircraft flight. The image is built up from the cross-track lines of pixels while the aircraft moves along. The image is taken in several narrow spectral bands, the appropriate choice and combination of which may allow for the detection of underwater objects.

The input to the model in this case consists of parameters such as across-track field-of-view, number of across-track pixels, aircraft altitude, speed and headings, and spectral bands. Environmental parameters include wind speed, parameters of the bio-optical model or the spectral optical properties of water, sun altitude and azimuth, bottom depth and profile. The other parameters include target shape, reflectance, and position with respect to image centre. One of the output files contains spectral radiances at specified spectral bands, interleaved by pixel. The file can be read by standard processing software such as ENVI.

Figure 24 shows an example of a simulated image and the result of simple processing in ENVI using the ratio of the band at 530 nm (green) to the band at 470 nm (blue). The direction of flight is from the right-hand side of the image to the left, wind is 5m/s at 45 degrees to the direction of flight, with the sun at 25 degrees above horizon right behind the aircraft. The bottom is sand with reflectivity varying linearly from 40% at 400 nm to 55% at 700 nm. Bottom depth varies from 8 m at the right end to

9.5 m at the left end. The aircraft altitude is 500 m, cross-track field of view is 40 degrees, resulting in a 364 m swath. There is a target in the middle of the surveyed area. The target is a grey rectangle 25m x 25m with 45% reflectance.

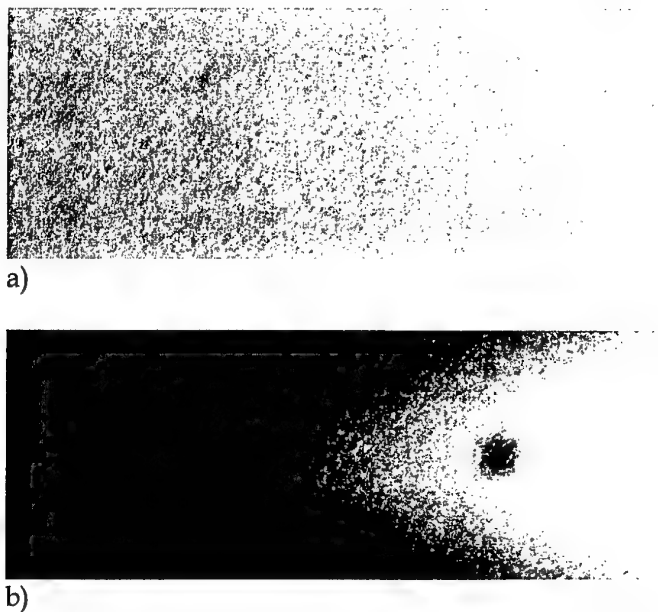


Figure 24. Example of simulated hyperspectral image. a) RGB "true colour" image; b) processed in ENVI using band ratio.

In this simulated case even the simple analysis allows us to see a target which is not visible in the conventional image. The processing also demonstrates that the shallower water the greener it appears which is in agreement with everyday experience.

11. Conclusion

A computer model has been developed to simulate the performance of passive optical imaging sensors, such as a human eye, a conventional digital camera or a hyperspectral sensor. The model is based on the ray tracing technique and implements several basic models describing various elements of image formation. These models are the analytical model of sun and sky radiance by Zibordi and Voss (1989) and the model of wind driven waves on sea surface based on the directional wave spectrum by Apel (1994). The sun and sky reflection by capillary waves on the sea surface is based on the model of Zeisse (1995). Optical properties of seawater are modelled by the one-parameter bio-optical model of Haltrin (1998). Several empirical and semi-empirical relations are used for describing such elements as radiance and irradiance transfer through a wavy sea surface, and image blur due to light scattering in ocean water. An

analytical expression for radiance scattered into a ray path has been developed in the present work.

All these models are based on approximations of various degrees of accuracy. Some of them were verified in the present work against other models and ground truth measurements. The model produces realistic images of sea surface and underwater targets but further verification of the simulation model and its components is required and is planned in the nearest future.

The future work will include comparison of simulations with hyperspectral data and ground truth measurements. Further improvements to the model elements will be made. It is planned to expand the model to incorporate simulation of the performance of active imaging systems such as Laser Range Gated (LRG) cameras and the Streak Tube Imaging Lidar (STIL). Also, atmospheric effects on light propagation near the sea surface will be included in the model.

12. Acknowledgments

The work presented in this report was sponsored by the Royal Australian Navy. The author also would like to thank Stuart Sutherland and Trevor Adams for productive discussions on model performance. Thanks to Ralph Abbot, Greg Schultz and Kevin Dyer for providing measurements of optical properties of seawater.

13. References

Angstrom, A. (1961). "Techniques of determining the turbidity of the atmosphere." *Tellus* **13**(2): 214-223.

Apel, J. R. (1994). "An improved model of the ocean surface wave vector spectrum and its effects on radar backscatter." *Journal of Geophysical Research* **99**(C8): 16269-91.

Carder, K. L., R. G. Stewart, G.R. Harvey, and P.B. Ortner (1989). "Marine humic and fulvic acids: Their effect on remote sensing of ocean chlorophyll." *Limnology and Oceanography* **34**(1): 68-81.

Cox, C. and W. Munk (1954). "Measurement of the Roughness of the Sea Surface from Photographs of the Sun's Glitter." *Journal of the Optical Society of America* **44**(11): 838-850.

Dierssen, H. M. and R. C. Smith (1997). "Estimation of irradiance just below the air-water interface." *Proc. SPIE* **2963**: 204-209.

Haltrin, V. I. (1998). "Self-consistent approach to the solution of the light transfer problem for irradiances in marine waters with arbitrary turbidity, depth, and surface

illumination. I. Case of absorption and elastic scattering." *Applied Optics* 37(18): 3773-84.

Haltrin, V. I. (1999). "Chlorophyll-based model of seawater optical properties." *Applied Optics* 38(33): 6826-32.

Iqbal, M. (1983). *An introduction to Solar radiation*. Toronto, Academic Press, 390p.

Jerlov, N. G. (1976). *Marine Optics*. Amsterdam, Elsevier, 231p.

Kasten, F. (1966). "A new table and approximate formula for relative optical air mass." *Arch. Meteorol. Geophys. Bioklimatol. Ser B* 14: 206-223.

Kattawar, G. W. (1975). "A three-parameter analytic phase function for multiple scattering calculations." *J. Quant. Spectrosc. Radiat. Transfer* 15(9): 839-849.

Kattawar, G. W. and C. N. Adams (1989). "Stokes vector calculations of the submarine light field in an atmosphere-ocean with scattering according to a Rayleigh phase matrix: Effect of interface refractive index on radiance and polarization." *Limnology Oceanography* 34(8): 1453-1472.

Kattawar, G. W. (1994). Polarization of light in the ocean. In: *Ocean Optics*. Ed. R. W. Spinrad, K. L. Carder and M. J. Perry, Oxford University Press: 202-275.

Kirk, J. T. O. (1984). "Dependence of relationship between inherent and apparent optical properties of water on solar altitude." *Limnology Oceanography* 29(2): 350-356.

Kirk, J. T. O. (1991). "Volume scattering function, average cosines, and the underwater light field." *Limnology Oceanography* 36(3): 455-467.

LeBlond, P. H. and L. A. Mysak (1978). *Waves in the ocean*. Amsterdam, Elsevier Scientific Publishing, 604p.

Lee, Z., K.L. Carder, C.D. Mobley, R.G. Steward, and J.S. Patch (1998). "Hyperspectral remote sensing for shallow waters. I. A semianalytical model." *Applied Optics* 37(27): 6329-6338.

Leckner, B. (1978). "The spectral distribution of solar radiation at the Earth's surface-elements of a model." *Solar Energy* 20(2): 143-50.

Massel, S. R. (1996). *Ocean surface waves: their physics and prediction*. Singapore, World Scientific, 491p.

Marggraf, W. A. and M. Griggs (1969). "Aircraft measurements and calculations of the total downward flux of solar radiation as a function of altitude." *J. Atmos. Sci.* **26**: 469-477.

Mobley, C. D. (1994). *Light and Water: Radiative Transfer in Natural Waters*. San Diego, Academic Press, 592p.

Morel, A. and B. Gentili (1993). "Diffuse reflectance of oceanic waters. II. Bidirectional aspects." *Applied Optics* **32**(33): 6864-6879.

Phillips, O. M. (1977). *The dynamics of the upper ocean*. Cambridge, Cambridge University Press, 336p.

Plass, G. N., G. Kattawar, and J. A. Guinn (1975). "Radiative transfer in the Earth's atmosphere and ocean: influence of ocean waves." *Applied Optics* **14**(8): 1924-36.

Pope, R. M. and E. S. Fry (1997). "Absorption spectrum (380-700 nm) of pure water. II. Integrating cavity measurements." *Applied Optics* **36**(33): 8710-23.

Preisendorfer, R. W. (1976). *Hydrologic Optics. Vol. 1: Introduction*. Honolulu, Hawaii, U.S. Department of Commerce, 218p.

Prieur, L. and S. Sathyendranath (1981). "An optical classification of coastal and oceanic waters based on the specific spectral absorption curves of phytoplankton pigments, dissolved organic matter, and other particulate materials." *Limnology Oceanography* **26**(4): 671-689.

Sathyendranath, S. and T. Platt (1997). "Analytic model of ocean color." *Applied Optics* **36**(12): p.2620-2629.

Sobolev, V. V. (1975). *Light Scattering in Planetary Atmospheres*. Oxford, Pergamon Press, 256 p.

Sutton, Ph. (1993). An electro-optical detection system for reflection free underwater images from aircraft. International Patent WO93/02367.

Vigroux, E. (1953). "Contribution à l'étude experimentale de l'absorption de l'ozone." *Ann. Phys.* **8**: 709-762.

Voss, K. J. (1991). "Simple empirical model of the oceanic point spread function." *Applied Optics* **30**(18): 2647-2651.

Zege, E. P., A. P. Ivanov, and I. L. Katsev. (1991). *Image Transfer through a Scattering Medium*. Berlin, Springer-Verlag, 349p.

Zeisse, C. R. (1995). "Radiance of the ocean horizon." *Journal of the Optical Society of America A-Optics & Image Science* **12**(9): pp. 2022-30.

Zibordi, G. and K. J. Voss(1989). "Geometrical and spectral distribution of sky radiance: comparison between simulations and field measurements." *Remote Sensing of Environment* **27**(3): 343-58.

Appendix A: Analytical Model of Sky Radiance

The following model for sky radiance is essentially from Zibordi and Voss (1989). Solar radiance just above the sea surface can be represented as the sum of two components: direct and diffuse radiance. The direct solar irradiance can be calculated using

$$E(\lambda) = E_{0D}(\lambda) \exp(-\tau(\lambda)m), \quad (A.1)$$

where $E_{0D}(\lambda)$ is the extraterrestrial solar irradiance corrected by the Sun-Earth distance:

$$E_{0D}(\lambda) = E_0(\lambda) \left(1 + \varepsilon \cos \frac{2\pi(D-3)}{365}\right)^2 \quad (A.2)$$

with $E_0(\lambda)$ being the extraterrestrial solar irradiance at wavelength λ , ε eccentricity of the Earth orbit, and D the Julian day. In equation (A.1) $\tau(\lambda)$ is the total optical thickness of the atmosphere, and m is the relative air mass (Kasten, 1966), which may be approximated as $1/\cos\theta_0$ for solar zenith angles (θ_0) less than 60° . For unit air mass,

$$\tau(\lambda) = \tau_R(\lambda) + \tau_A(\lambda) + \tau_{O_3}(\lambda) + \tau_W(\lambda) + \tau_G(\lambda) \quad (A.3)$$

Various optical thicknesses in the right hand side of equation (A.3) can be computed by various empirical equations as follows.

The scattering optical thickness of permanent gases (molecular, or Rayleigh, optical thickness) can be computed (Marggraf and Griggs, 1969) as

$$\tau_R(\lambda) = 0.0088\lambda^{-4.15+0.2\lambda}, \quad (A.4)$$

where λ is in units of micrometers.

The absorption and scattering optical thickness of aerosol, assuming a radius power law distribution of particles, can be given by (Ångstrom, 1961)

$$\tau_A(\lambda) = \alpha\lambda^{-\beta}, \quad (A.5)$$

where α and β respectively relate to the concentration and size distribution of particles. Typical values of the wavelength coefficient β lie in the range 0.8 - 2.

Turbidity coefficient α can be calculated as $\alpha = \alpha_0 0.5^{\beta-1.3}$. Typical values of the Ångström turbidity coefficient α_0 are given in Table 1.

Table 1. Typical Ångström turbidity coefficients (Leckner, 1978)

Latitude	60°N	45°N	30°N	0°
Low limit	0.01	0.047	0.047	0.047
Medium	0.057	0.077	0.097	0.117
High limit	0.093	0.187	0.375	0.375

The absorption optical thickness of ozone can be computed through

$$\tau_{O_3}(\lambda) = C_{O_3} K_{O_3}(\lambda), \quad (A.6)$$

where $K_{O_3}(\lambda)$ (cm⁻¹) is the spectral absorption coefficient of the ozone (Table 2, Vigroux, 1953) and C_{O_3} (cm) is the ozone concentration.

Table 2. Spectral absorption coefficient of ozone (Vigroux, 1953).

λ	K_{O_3}								
290	38	445	0.003	515	0.045	585	0.118	700	0.023
295	20	450	0.003	520	0.048	590	0.115	710	0.018
300	10	455	0.004	525	0.057	595	0.12	720	0.014
305	4.8	460	0.006	530	0.063	600	0.125	730	0.011
310	2.7	465	0.008	535	0.07	605	0.13	740	0.01
315	1.35	470	0.009	540	0.075	610	0.12	750	0.009
320	0.8	475	0.012	545	0.08	620	0.105	760	0.007
325	0.38	480	0.014	550	0.085	630	0.09	770	0.004
330	0.16	485	0.017	555	0.095	640	0.079	780	0
335	0.075	490	0.021	560	0.103	650	0.067	790	0
340	0.04	495	0.025	565	0.11	660	0.057	800	0
345	0.019	500	0.03	570	0.12	670	0.048	810	0
350	0.007	505	0.035	575	0.122	680	0.036	820	0
355	0	510	0.04	580	0.12	690	0.028	830	0

The absorption optical thickness of water vapour (Iqbal, 1983) can be calculated by

$$\tau_w(\lambda) = \frac{0.2385 K_w(\lambda) C_w}{(1 + 20.07 K_w(\lambda) C_w)^{0.45}}, \quad (A.7)$$

where $K_w(\lambda)$ (cm⁻¹) is the spectral absorption coefficient of water vapour (Leckner, 1978) and C_w (cm) is the precipitable water of the atmosphere.

The absorption optical thickness of the so-called uniformly-mixed gases (mainly oxygen and carbon dioxide) can be calculated (Iqbal, 1983) by

$$\tau_g(\lambda) = \frac{1.41K_g(\lambda)}{[1+118.93K_g(\lambda)]^{0.45}}, \quad (\text{A.8})$$

where $K_g(\lambda)$ is the effective absorption coefficient (Leckner, 1978). In the visual part of the spectrum the water vapour absorption and the uniformly-mixed gases absorption can be neglected.

The diffuse part of the solar radiance is due to scattering of sun light by particles and molecules in the atmosphere. For computation of the diffuse radiance it is necessary to separate the total aerosol optical thickness $\tau_a(\lambda)$ into its scattering $\tau_{as}(\lambda)$ and absorption $\tau_{aa}(\lambda)$ components:

$$\tau_a(\lambda) = \tau_{as}(\lambda) + \tau_{aa}(\lambda). \quad (\text{A.9})$$

This can be done through the aerosol single scattering albedo $\omega_a(\lambda)$, which is the ratio of energy scattered to total attenuation by aerosol, and defined by

$$\omega_a(\lambda) = \frac{\tau_{as}(\lambda)}{\tau_a(\lambda)}, \quad (\text{A.10})$$

so that

$$\tau_{as}(\lambda) = \omega_a(\lambda)\tau_a(\lambda), \quad (\text{A.11})$$

$$\tau_{aa}(\lambda) = [1 - \omega_a(\lambda)]\tau_a(\lambda). \quad (\text{A.12})$$

$\omega_a(\lambda)$ strongly depends on the optical properties of the aerosol particles. Generally it is assumed invariant with wavelength in the visible and near infrared and ranges between 0.6 and 1.0, with $\omega_a \approx 0.6$ for urban/industrial aerosol, $\omega_a \approx 0.9$ for continental aerosol and $\omega_a \approx 1.0$ (pure scattering) for maritime aerosol (Zege *et al.*, 1991).

The phase function defines the angular distribution of sky radiance due to scattering of diffusing constituents. The molecular component (Rayleigh scattering) is given by the classical relationship for isotropic scattering

$$P_R(\Psi) = \frac{3}{4}(1 + \cos^2 \Psi), \quad (A.13)$$

where Ψ is the scattering angle.

The aerosol phase function can be approximated by the Two Term Henyey-Greenstein (TTHG) analytical function

$$P_A(\Psi) = \frac{(1 - g_1^2)a}{(1 + g_1^2 - 2g_1 \cos \Psi)^{1.5}} + \frac{(1 - g_2^2)(1 - a)}{(1 + g_2^2 + 2g_2 \cos \Psi)^{1.5}}, \quad (A.14)$$

where parameters a , g_1 , and g_2 (asymmetry factors) depend on the aerosol size distribution and wavelength, however, the latter is less significant. The asymmetry parameters for the TTHG function ($a=0.962$, $g_1=0.713$, and $g_2=0.759$) were taken from Kattawar (1975). These values were successfully used in remote sensing applications with clear sky conditions (Gordon et al., 1983).

The global phase function of the atmosphere is given by

$$P(\Psi) = \frac{\tau_R(\lambda)P_R(\Psi) + \tau_{As}(\lambda)P_A(\Psi)}{\tau_R(\lambda) + \tau_{As}(\lambda)}, \quad (A.15)$$

with the normalisation condition

$$\frac{1}{2} \int_0^\pi P(\Psi) \sin \Psi d\Psi = 1, \quad (A.16)$$

and the scattering angle Ψ for sky radiance defined by

$$\Psi = \arccos(\cos \theta \cos \theta_0 - \sin \theta \sin \theta_0 \cos(\phi - \phi_0)). \quad (A.17)$$

where θ_0, ϕ_0 and θ, ϕ are the sun and sensor zenith and azimuth, respectively.

Calculation of sky radiance is based on the approximate solution of the radiative transfer equation given by Sobolev (1975) for a plane parallel, homogeneous and cloudless atmosphere bounded by a lambertian surface. This solution allows the exact computation of the first order of scattering, while multiple orders are accounted for through the phase function averaged over the azimuth. Absorbing constituents are assumed condensed in a thick layer at the top of the atmosphere, which enables independent computation of absorbing and scattering processes. In such a situation the sky radiance can be given by

$$L_{sky}(\lambda) = \frac{E_{0D}(\lambda)}{\pi} \sigma(\tau_d(\lambda)) \cos \theta_0 \exp \left[\frac{-\tau_a(\lambda)}{\cos \theta_0} \right], \quad (A.18)$$

where $\tau_d(\lambda)$ and $\tau_a(\lambda)$ are the total optical thickness for scattering and absorbing constituents, respectively, and are given by

$$\tau_d(\lambda) = \tau_R(\lambda) + \tau_{As}(\lambda), \quad (A.19)$$

$$\tau_a(\lambda) = \tau_{O_3}(\lambda) + \tau_W(\lambda) + \tau_G(\lambda) + \tau_{Aa}(\lambda). \quad (A.20)$$

The term $\sigma(\tau_d(\lambda))$ is the scattering transmission coefficient of the atmosphere and, following Sobolev (1975), is given by

$$\begin{aligned} \sigma(\tau_d(\lambda)) = & \frac{\{[1 - \rho(\lambda)]R(\lambda, \theta) + 2\rho(\lambda)\}R(\lambda, \theta_0)}{4 + (3 - P_1)[1 - \rho(\lambda)]\tau_d(\lambda)} \\ & - \frac{1}{2} \left(\exp \frac{-\tau_d(\lambda)}{\cos \theta} + \exp \frac{-\tau_d(\lambda)}{\cos \theta_0} \right) \\ & + [P(\Psi) - (3 + P_1)\cos \theta \cos \theta_0] \sigma_1(\tau_d(\lambda)), \end{aligned} \quad (A.21)$$

where the term $\sigma_1(\tau_d(\lambda))$ expresses the single scattering transmission

$$\sigma_1(\tau_d(\lambda)) = \frac{1}{4} \frac{\exp \frac{-\tau_d(\lambda)}{\cos \theta} - \exp \frac{-\tau_d(\lambda)}{\cos \theta_0}}{\cos \theta - \cos \theta_0}, \quad (\theta \neq \theta_0), \quad (A.22)$$

P_1 is the first term in the Legendre polynomial expansion of the phase function

$$P_1 = \frac{3}{2} \int_0^\pi P(\Psi) \cos \Psi \sin \Psi d\Psi, \quad (A.23)$$

$R(\lambda, \zeta)$ (with $\zeta = \theta, \theta_0$) is an auxiliary function

$$R(\lambda, \zeta) = 1 + \frac{3}{2} \cos \zeta + \left(1 - \frac{3}{2} \cos \zeta \right) \exp \left[\frac{-\tau_d(\lambda)}{\cos \zeta} \right], \quad (A.24)$$

and $\rho(\lambda)$ is spectral albedo of the surface (assumed lambertian).

Appendix B: Wavenumber Spectrum

Here we present a short summary of the Apel's directional wavenumber spectrum following Apel (1994). The spectrum can be written as follows:

$$\Psi(k) = \psi(k)D(k, \phi), \quad (B.1)$$

where k is the wavenumber and ϕ is the azimuth angle. $\psi(k)$ is the portion of the spectrum that is independent on the azimuth angle, ϕ . It can be represented as a multiplication of the five factors:

$$\psi(k) = A \cdot L_o \cdot J_p \cdot k^{-4} \cdot H_i \quad (B.2)$$

Here, the spectral constant

$$A = 0.00195, \quad (B.3)$$

the low-frequency roll-off

$$L_o = \exp[-(k_p/k)^2], \quad (B.4)$$

where

$$k_p = \frac{g}{\sqrt{2}u^2} \quad (B.5)$$

with g being the specific gravity and u the wind speed measured at ten metres height above sea surface.

The spectral peak

$$J_p(k) = \Gamma^{\exp\left[-\left(\frac{k\gamma_2 - k_p\gamma_2}{2\delta^2 k_p}\right)^2\right]}. \quad (B.6)$$

For fully developed seas, the base, Γ , is 1.7, and the width parameter of the spectral peak, δ , is 0.40.

A combination of high frequency effects is given by

$$H_i = [R_{ro} + S \cdot R_{res}] \cdot V_{dis}, \quad (B.7)$$

where

$$R_{ro} = \frac{1}{1 + (k/k_{ro})^2}, \text{ with } k_{ro} = 100 \text{ rad/m.} \quad (\text{B.8})$$

$$R_{res} = ak \operatorname{sech}[(k - k_{res})/k_w], \text{ with } a=0.8; k_{res}=400; k_w=450. \quad (\text{B.9})$$

$$S(u) = \exp \left\{ s_1 + s_2 \left(1 - e^{-u/u_\eta} \right) \right\} \ln_e 10, \quad (\text{B.10})$$

where $s_1 = -4.95$, $s_2 = 3.45$, and $u_\eta = 4.7 \text{ m/s}$

$$V_{dis} = \exp(-k^2/k_{dis}^2), \quad k_{dis} \approx 6283. \quad (\text{B.11})$$

The directional part of the spectrum is:

$$D(k, \phi) = \exp \left[\frac{-(\phi - \phi_u)^2}{2\phi_s^2(k)} \right], \quad (\text{B.12})$$

$$2\phi_s^2(k) = [0.14 + 5.0(k/k_p)^{-1.3}]^{-1}, \quad (\text{B.13})$$

where ϕ_u is the wind direction.

Appendix C: Bio-Optical Model

This Appendix presents a summary of the one-parameter bio-optical model of Haltrin (1999). Absorption is described as the sum of absorption coefficients of pure water, chlorophyll, and two components of Dissolved Organic Matter (DOM): fulvic and humic acids:

$$a(\lambda) = a_w(\lambda) + 0.06a_c^0(\lambda)(C_c/C_c^0)^{0.602} + a_f^0 C_f \exp(-k_f \lambda) + a_h^0 C_h \exp(-k_h \lambda), \quad (C.1)$$

where $a_w(\lambda)$ is the absorption coefficient of pure water in m^{-1} (Pope and Fry, 1997), λ is the vacuum wavelength in nm , $a_c^0(\lambda)$ is the specific absorption coefficient of chlorophyll in m^{-1} (Prieur and Sathyendranath, 1981), C_c is the total concentration of chlorophyll in mg/m^3 ($C_c^0 = 1mg/m^3$), $a_f^0 = 35.959m^2/mg$ is the specific absorption coefficient of fulvic acid, $k_f = 0.0189nm^{-1}$; $a_h^0 = 18.828m^2/mg$ is the specific absorption coefficient of humic acid, $k_h = 0.01105nm^{-1}$; C_f and C_h are, respectively, concentrations of fulvic and humic acids in mg/m^3 (Carder *et al.*, 1989).

The scattering coefficient $b(\lambda)$ and backscattering coefficient $b_B(\lambda)$ are calculated according to following equations (Haltrin, 1999):

$$b(\lambda) = b_w(\lambda) + b_s^0(\lambda)C_s + b_l^0(\lambda)C_l, \quad (C.2)$$

$$b_B(\lambda) = 0.5b_w(\lambda) + B_s b_s^0(\lambda)C_s + B_l b_l^0(\lambda)C_l, \quad (C.3)$$

here

$$B_s = 0.5 \int_{\pi/2}^{\pi} p_s(\theta) \sin \theta d\theta = 0.039, \quad B_l = 0.5 \int_{\pi/2}^{\pi} p_l(\theta) \sin \theta d\theta = 6.4 \cdot 10^{-4}, \quad (C.4)$$

B_s is the probability of backscattering by small particles, B_l is the probability of backscattering by large particles, $b_w(\lambda)$ is the scattering coefficient by pure water in m^{-1} , $b_s^0(\lambda)$ and $b_l^0(\lambda)$ are, respectively, the specific scattering coefficients in m^2/g for small and large particulate matter, C_s and C_l are, respectively, concentrations in g/m^3 of small and large particles. The following equations are given by Haltrin (1999):

$$b_w(\lambda) = (5.826 \cdot 10^{-3} m^{-1}) \left(\frac{400}{\lambda} \right)^{4.322}, \quad (C.5)$$

$$b_s^0(\lambda) = (1.1513m^{2/g}) \left(\frac{400}{\lambda} \right)^{1.7} \quad (C.6)$$

$$b_l^0(\lambda) = (0.3411m^2/g) \left(\frac{400}{\lambda} \right)^{0.3} \quad (C.7)$$

Haltrin (1999) finds, from experimental data of other researchers, that all five concentrations in above equations correlate with each other and suggests using the concentration of chlorophyll as the main parameter and express other concentrations as follows:

$$C_f = 1.74098 \cdot C_c \cdot \exp(0.12327 \cdot C_c) \quad (C.8)$$

$$C_h = 0.19334 \cdot C_c \cdot \exp(0.12343 \cdot C_c) \quad (C.9)$$

$$C_s = 0.01739 \cdot C_c \cdot \exp(0.11631 \cdot C_c) \quad (C.10)$$

$$C_l = 0.76284 \cdot C_c \cdot \exp(0.03092 \cdot C_c) \quad (C.11)$$

DISTRIBUTION LIST

Simulation of Passive Imaging of Underwater Objects

Alexei Kouzoubov

AUSTRALIA

DEFENCE ORGANISATION

Task Sponsor	DNW	2 copies
--------------	-----	----------

S&T Program

Chief Defence Scientist	}	shared copy
FAS Science Policy		
AS Science Corporate Management		
Director General Science Policy Development		
Counsellor Defence Science, London (Doc Data Sheet)		
Counsellor Defence Science, Washington (Doc Data Sheet)		
Scientific Adviser Joint		
Navy Scientific Adviser		
Scientific Adviser - Army (Doc Data Sheet and distribution list only)		
Air Force Scientific Adviser (Doc Data Sheet and distribution list only)		
Director Trials (Doc Data Sheet and distribution list only)		

Aeronautical and Maritime Research Laboratory

Director

Chief of Maritime Operations Division
Research Leader, Mine Warfare
Research Leader, Maritime Sensor Systems
Head Maritime Optronics
Author(s): A.Kouzoubov
V.K.Shettigara
S.Sutherland
P.Chapple
P.Mulhearn

2 copies

DSTO Library

Library Fishermans Bend	(Doc Data sheet only)
Library Maribyrnong	(Doc Data sheet only)
Library Edinburgh	
Australian Archives	
Library, MOD, Pyrmont	
Library, MOD, HMAS Stirling	
*US Defense Technical Information Centre,	2
*UK Defence Research Information Center,	2
*Canada Defence Scientific Information Service,	1

Capability Development Division

Director General Aerospace Development (Doc Data Sheet only)
Director General Maritime Development

Knowledge Staff

Director General Command, Control, Communications and Computers (DGC4)
(Doc Data Sheet only)

Navy

SO (Science), Director of Naval Warfare, Maritime Headquarters Annex,
Garden Island, NSW 2000. (Doc Data Sheet only)

Intelligence Program

DGSTA Defence Intelligence Organisation
Manager, Information Centre, Defence Intelligence Organisation

Corporate Support Program

Library Manager, DLS-Canberra

UNIVERSITIES AND COLLEGES

Australian Defence Force Academy
Library
Head of Aerospace and Mechanical Engineering
Serials Section (M list), Deakin University Library, Geelong, 3217
Hargrave Library, Monash University (Doc Data Sheet only)
Librarian, Flinders University

OUTSIDE AUSTRALIA

ABSTRACTING AND INFORMATION ORGANISATIONS

Engineering Societies Library, US
Documents Librarian, The Center for Research Libraries, US

INFORMATION EXCHANGE AGREEMENT PARTNERS

Acquisitions Unit, Science Reference and Information Service, UK
Library - Exchange Desk, National Institute of Standards and Technology, US

SPARES

5

Total number of copies:

44

DEFENCE SCIENCE AND TECHNOLOGY ORGANISATION DOCUMENT CONTROL DATA		1. PRIVACY MARKING/CAVEAT (OF DOCUMENT)		
2. TITLE Simulation of Passive Imaging of Underwater Objects		3. SECURITY CLASSIFICATION (FOR UNCLASSIFIED REPORTS THAT ARE LIMITED RELEASE USE (L) NEXT TO DOCUMENT CLASSIFICATION) Document (U) Title (U) Abstract (U)		
4. AUTHOR(S) A. Kouzoubov		5. CORPORATE AUTHOR Aeronautical and Maritime Research Laboratory 506 Lorimer St Fishermans Bend Victoria 3207 Australia		
6a. DSTO NUMBER DSTO-TR-1240	6b. AR NUMBER AR-012-070	6c. TYPE OF REPORT Technical Report	7. DOCUMENT DATE November 2001	
8. FILE NUMBER 9505-21-84	9. TASK NUMBER NAV99/062	10. TASK SPONSOR DNW	11. NO. OF PAGES 46	12. NO. OF REFERENCES 35
13. URL on the World Wide http://www.dsto.defence.gov.au/corporate/reports/DSTO-TR-1240.pdf			14. RELEASE AUTHORITY Chief, Maritime Operations Division	
15. SECONDARY RELEASE STATEMENT OF THIS DOCUMENT <i>Approved for public release</i>				
OVERSEAS ENQUIRIES OUTSIDE STATED LIMITATIONS SHOULD BE REFERRED THROUGH DOCUMENT EXCHANGE, PO BOX 1500, SALISBURY, SA 5108				
16. DELIBERATE ANNOUNCEMENT No Limitations				
17. CASUAL ANNOUNCEMENT Yes 18. DEFTEST DESCRIPTORS				
Computerized simulation, Imaging techniques, Underwater objects, Spectral reflectance, Air water interactions, Ray tracing, Radiance, Irradiance, Mine hunting				
19. ABSTRACT A computer model simulating performance of passive optical sensors for imaging underwater objects from above-water platforms is described. The model is based on the models of sun and sky spectral radiance, wavy sea surface, light propagation in seawater and is able to render images of underwater objects as seen through the air-water interface.				